https://doi.org/10.5194/egusphere-2026-2400
Preprint. Discussion started: 30 April 2026

A New Method for Retrieving Momentum Flux Magnitude from Multiple Gravity Wave Signals Using GNSS Radio Occultation Profile Triples

Jialiang Hou[1], Jia Luo[1,2], Xiaohua Xu[1]

[1]School of Geodesy and Geomatics, Wuhan University, Wuhan, 430079, China
[2]Key Laboratory of Geospace Environment and Geodesy, Ministry of Education, Wuhan, 430079, China

Correspondence to: Jia Luo (jialuo@whu.edu.cn) and Xiaohua Xu (xhxu@sgg.whu.edu.cn)

Abstract. Gravity wave (GW) momentum flux (MF) is a key parameter characterizing GW energy transport in the atmosphere, but extracting GW MF from satellite observations remains challenging. Here, we propose a new method for retrieving GW MF magnitude using Global Navigation Satellite System (GNSS) radio occultation (RO) temperature profile triples. Unlike the traditional profile-triple-based method, which only considers the dominant vertical wavelength of the largest-amplitude wave signal, the new method takes into account a set of significant vertical wavelengths determined by an empirical threshold. This threshold is optimized to balance the completeness of MF information and the reliability of GW signals. Experiments are conducted using COSMIC-2 RO dry temperature data. Qualified triples are classified into Type A (triples meeting the criteria of both the new and the traditional methods) and Type B (triples meeting only the new method's criteria). At most latitudes between 40°S and 40°N, the zonal-mean total MF from Type B triples exceeds that from Type A, with a pronounced peak at around 20°N. The contribution of primary wave signals to the total MF magnitude is significantly lower at the altitude range of 20–25 km than at higher altitudes, likely attributable to frequent wave-breaking processes and the generation of secondary GWs within 20–25 km. Compared with the traditional method, the new method significantly improves the data utilization rate of profile triples and enables a more complete measurement of the total GW MF magnitude which may originate from different sources.

1 Introduction

Gravity waves (GWs) are one of the fundamental oscillations in the atmosphere, generated by buoyancy and gravity under stable atmospheric stratification. They transmit energy, momentum, atmospheric constituents, and water vapor in fluid environments, and influence atmospheric states through energy deposition during propagation (John and Kumar, 2012; Hindley et al., 2015; Zhang et al., 2015). As a key component of the atmospheric system, GWs play a significant driving role in the circulation of the middle and lower atmosphere through wave drag and propagation processes, exerting a non-negligible influence on the evolution of global circulation (Holton, 1983; Fritts and Alexander, 2003). Therefore, accurately

https://doi.org/10.5194/egusphere-2026-2400
Preprint. Discussion started: 30 April 2026

representing GW processes in climate models is essential for enhancing the physical consistency and predictive capability of simulations (Kim et al., 2003; Alexander and Shepherd, 2010; Alexander et al., 2010).

To optimize the GW parameterization schemes, it is essential to provide effective observational constraints, which relies on the support of high-quality global observational data (Fritts and Alexander, 2003; Meriwether and Gerrard, 2004; Liu et al., 2017). The satellite remote sensing technology of Global Navigation Satellite System (GNSS) radio occultation (RO) has become an effective technique for detecting atmospheric GW activity, especially in the upper troposphere and lower stratosphere (UTLS) region, owing to the temperature profiles provided by GNSS RO observations, which are with global coverage, high vertical resolution, and long-term stability (Kursinski et al., 1997; Tsuda et al., 2000; Ratnam et al., 2004; Steiner and Kirchengast, 2005; Horinouchi and Tsuda, 2009; Hindley et al., 2015).

GW momentum flux (MF) is a key parameter characterizing GW energy transport and wave-mean flow interactions, directly influencing atmospheric circulation structures and mesospheric/ stratospheric dynamical processes (Holton, 1982; Fritts and Alexander, 2003; Ern et al., 2004). However, retrieving GW MF from RO temperature profiles remains challenging. Some scholars proposed to derive GW MF using RO temperature profile pairs (Wang and Alexander, 2010; Ern et al., 2011; Hindley et al., 2015), while the horizontal wavelengths derived from RO profile pairs are merely "apparent" horizontal wavelengths along the line connecting the two measurement points, from which the actual horizontal wavelength can differ significantly, with the specific discrepancy depending on the angle θ between this connecting line and the true wave's propagation direction. Specifically, the apparent wavelength is larger than the true wavelength by a factor of $1/cos\theta$ (Alexander et al., 2008; Faber et al., 2013; Schmidt et al., 2016), which means that the apparent horizontal wavelength systematically deviates from the true one, ultimately introducing biases in both the magnitude and the direction of the retrieved GW MF. To address this issue, the profile-triple-based method had been brought forward as a replacement for the profile pair method, which is of the ability to extract the horizontal wavelength and MF magnitude of GWs more accurately (Faber et al., 2013; Schmidt et al., 2016; Zeng et al., 2021).

On the other hand, as pointed out by Fritts and Alexander (2003), the GW fluctuating field consists of multi-scale wave superimpositions in theory, though an actual wave spectrum is often dominated by a single or a few large-amplitude modes. Traditional methods for retrieving GW MF typically consider only the dominant vertical wavelength component with the largest amplitude, thereby neglecting the contributions from other wave signals. These overlooked non-dominant wave components may sometimes contribute to even larger MF (Andrews et al., 1987; Fritts and Alexander, 2003; Wright and Gille, 2013). Wright and Gille (2013) proposed a new method for retrieving GW MF based on multiple wave signals, and they found that in the 20–30 km altitude range, the GW MF magnitude retrieved by their method is overall 68% larger than those obtained by traditional methods, with particularly significant improvements in tropical regions. However, their method still relies on the profile-pair retrieval framework and fails to overcome the systematic bias introduced by the apparent horizontal wavelength.

To address the above limitations of existing GW MF retrieval methods, this paper proposes a novel method for retrieving multi-wave signal MF magnitude based on GNSS RO temperature profile triples, which not only avoids the

https://doi.org/10.5194/egusphere-2026-2400
Preprint. Discussion started: 30 April 2026

systematic biases introduced by profile-pair-based retrievals, but also overcomes the limitation of extracting only the maximum amplitude wave signal under the single-wave assumption. The proposed method can capture the contributions of multi-scale GW signals corresponding to multiple vertical wavelengths to the MF magnitude, thereby enhancing the informational completeness of the retrieval results, and it can also effectively utilize a large number of profile triples that were previously discarded by traditional profile-triple-based approach, significantly improving the data utilization rate. Section 2 provides a brief introduction to the GNSS RO data used. Section 3 details the principles of the proposed method for retrieving GW MF magnitude. Section 4 analyses the differences between the proposed method and the existing profile-triple-based method. Section 5 presents the experimental results and discussion, and conclusions are drawn in Section 6.

2 Data

This study utilizes the "atmPrf" dry temperature profiles from the Constellation Observing System for Meteorology, Ionosphere, and Climate-2 (COSMIC-2) RO mission (Version 0001.0001) during June–August 2020, provided by the COSMIC Data Analysis and Archive Center (CDAAC). The time period of June–August corresponds to the Northern Hemisphere (NH) summer, which features a diversity of GW sources in mid and low latitudes, including interactions between monsoon flows and topography, convection, and shear effects associated with jets (Fritts and Alexander, 2003; Ratnam et al., 2008; Wright and Gille, 2013; Randel et al., 2021), facilitating the detection of GW signals with different vertical wavelengths and the validation of our newly proposed method. The COSMIC-2 mission system consists of a constellation of six satellites deployed in low-Earth orbits at an altitude of approximately 550 km with an inclination of 24° (Schreiner et al., 2020; Pedatella et al., 2021). It is capable of observing both Global Positioning System (GPS) and Global Navigation Satellite System (GLONASS) RO events and can provide approximately 5,000 RO temperature profiles daily in the low and mid latitude regions (Anthes and Schreiner, 2019; Schreiner et al., 2020). The COSMIC-2 dry temperature profiles have the advantage of high vertical resolution and high accuracy in the upper troposphere-lower stratosphere region (Randel et al., 2021; Babu and Liou, 2022). In this work, COSMIC-2 dry temperature profiles are used to retrieve the GW MF magnitudes in the lower stratosphere at altitudes of 20–35 km.

3 Method

This section systematically describes the procedures of the multi-wave signal GW MF retrieval method based on temperature profile triples proposed in this study. To ensure data quality, raw dry RO temperature profiles are screened based on the "bad" global attribute in the "atmPrf" files, eliminating all invalid profiles with an attribute value of "1". For the data kept after screening, the subsequent processing procedures include perturbation temperature extraction, triple matching, wave spectrum analysis, and the calculations of horizontal wavelength and MF magnitude of GW.

https://doi.org/10.5194/egusphere-2026-2400
Preprint. Discussion started: 30 April 2026

3.1 Extraction of Perturbation Temperature

In this study, we apply the single-point detrending method using Savitzky–Golay filter (Savitzky and Golay, 1964), as proposed by Hindley et al. (2015), to extract temperature perturbation profiles from the original RO temperature profiles in the 10–50 km altitude range (i.e., the upper troposphere to the stratosphere), where GW activity is significant. The extracted profiles are obtained at a 0.1 km vertical resolution. By processing each profile independently, this method ensures that the extracted GW signals reflect local atmospheric structures and are regionally representative. As noted by Hindley et al. (2015), this method exhibits higher sensitivity to GW signals with vertical wavelengths of 4–13 km. See Hindley et al. (2015) for further details.

3.2 Spatiotemporal Constraints for the Profile Triples

After deriving the perturbation temperature profiles from all the valid original temperature profiles, the perturbation temperature profile triples are selected under specific spatiotemporal constraints (Faber et al., 2013; Schmidt et al., 2016). To ensure that the three profiles within each triple capture the same GW signals while simultaneously maintaining a sufficient number of triples for GW MF calculations, the spatiotemporal constraints defined by Zeng et al. (2021) are adopted, i.e., any two profiles within a triple must have a temporal separation ≤ 20 minutes and a spatial distance ≤ 600 km. Additionally, following Schmidt et al. (2016), the minimum spatial separation between any two profiles in a triple must exceed the latitude (φ)-dependent minimum horizontal sampling distance, calculated using Equation (1):

$$\Delta x_{\min} = 70 + 30 \cdot \cos(2\varphi) \tag{1}$$

Under these combined constraints, all the profile triples are extracted, and the final selected profile triples exhibit inter-profile temporal differences ≤ 20 minutes and spatial separations of 40–600 km.

3.3 Determination of Initial Set of Significant Vertical Wavelengths through Wave Spectrum Analysis

For each temperature perturbation profile triple, wave spectrum analysis is further conducted to derive its initial set of significant vertical wavelengths (SVWs) at each altitude. Figure 1 illustrates an example for deriving the initial set of SVWs at a given altitude z from a triple composed of Profiles 1, 2 and 3, and the detailed steps are as follows:

(1) Following Faber et al. (2013) and Schmidt et al. (2016), the discrete Morlet wavelet transform is applied individually to each temperature perturbation profile within the triple. At the given altitude z, this analysis yields the amplitudes of the wave signals corresponding to a discrete set of vertical wavelengths $\lambda = \{\lambda_1, \lambda_2, \dots, \lambda_j, \dots, \lambda_m\}$, and the three amplitude curves derived from the three temperature perturbation profiles are respectively shown as the red, green, and blue solid lines in Figure 1(a). On the amplitude curve for Profile i ($i = 1, 2$ or 3), the amplitude of the wave signal corresponding the vertical wavelength λ_j is denoted as $A(\lambda_j, i)$, and the maximum value among $A(\lambda_j, i)$ ($j = 1, 2, \dots, m$) is denoted as $A_{max,i}$. The discrete wavelength sequence λ is determined by the altitude range (10–50 km) and the vertical

https://doi.org/10.5194/egusphere-2026-2400
Preprint. Discussion started: 30 April 2026

resolution (0.1 km) of the temperature perturbation profiles, with its generation principle detailed in Torrence and Compo (1998), and the altitude z is set as 25 km in this example.

(2) On the amplitude curve for Profile i ($i = 1, 2$ or 3), for a given empirical threshold α, the high-amplitude vertical wavelength ranges (HAVWRs) are defined as the vertical wavelength ranges within which all the discrete vertical wavelengths correspond to wave signals with amplitudes no less than $\alpha \cdot A_{max,i}$. In Figure 1(a), with α set as 0.6, the red, green, and blue dashed lines respectively represent the HAVWRs on the amplitude curves for Profile 1, Profile 2, and Profile 3. The intersections of the HAVWRs of the three amplitude curves yield the HAVWRs for the triple. As shown in Figure 1(a), the HAVWRs for the given triple at the altitude of 25 km comprise two sub-ranges: r_1 and r_2.

(3) Subsequently, cross-spectrum analysis is performed on each of the three profile pairs within the temperature perturbation triple, also using the discrete Morlet wavelet method. At the given altitude z, this procedure yields three co-amplitude curves as a function of vertical wavelength, shown by the red, green, and blue solid lines in Figure 1(b). For the principle of cross-spectrum analysis, see Alexander et al. (2008).

(4) For each co-amplitude curve, all discrete vertical wavelengths that satisfy two conditions (i.e., corresponding to wave signals with local amplitude maxima and at the same time falling within the triple's HAVWRs), are identified and assigned to the initial set of SVWs, which is denoted as SVWs $= \{\lambda_{v,1},\ \lambda_{v,2}, \dots, \lambda_{v,l}, \dots, \lambda_{v,n}\}$, with n representing the total number of the identified initial SVWs. In the example presented in Figure 1, with $\alpha = 0.6$, the initial set of SVWs at the altitude of 25 km is obtained as $\{\lambda_{v,1},\ \lambda_{v,2}\}$, in which $\lambda_{v,1}$= 8.54 km and $\lambda_{v,2}$= 12.80 km, as shown in Figure 1(b).

https://doi.org/10.5194/egusphere-2026-2400
Preprint. Discussion started: 30 April 2026

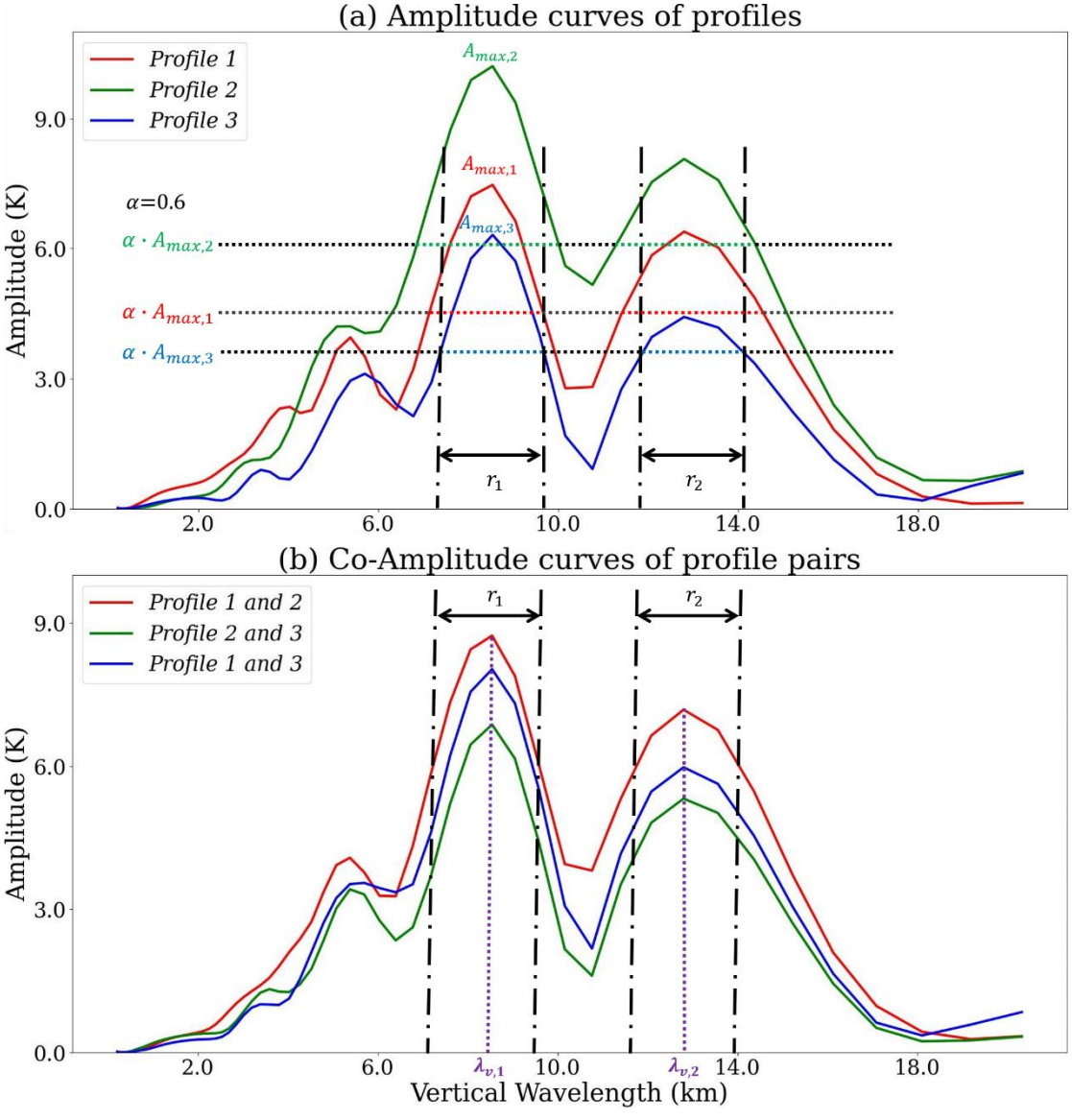

Figure 1: An example for identifying the initial set of significant vertical wavelengths at a given altitude from a profile triple.

3.4 Calculation of Horizontal Wavelength and Momentum Flux Magnitude

For a given temperature perturbation profile triple, at a given altitude z, the horizontal wavelength $\lambda_{h,l}$ corresponding to each vertical wavelength $\lambda_{v,l}$ $(l = 1, 2, \ldots, n)$ within the initial set of SVWs is derived subsequently. Using Profile 1 as the reference, the phase differences for the wave signal between the pair of Profile 1 and Profile 2, and that between the pair of Profile 1 and Profile 3, which are both of vertical wavelength $\lambda_{v,l}$, are denoted as $\Delta\phi_{12}(\lambda_{v,l})$ and $\Delta\phi_{13}(\lambda_{v,l})$, respectively.

https://doi.org/10.5194/egusphere-2026-2400
Preprint. Discussion started: 30 April 2026

According to Faber et al. (2013) and Schmidt et al. (2016), when the three profiles within the triple satisfy the strict spatiotemporal constraints, the relationship between the phase differences and the horizontal wavenumber components can be established using Equations (2) and (3):

$$\Delta\phi_{12}(\lambda_{v,l}) = k_{x,l\_1}\cdot(x_1 - x_2) + k_{y,l\_1}\cdot(y_1 - y_2) \tag{2}$$

$$\Delta\phi_{13}(\lambda_{v,l}) = k_{x,l\_1}\cdot(x_1 - x_3) + k_{y,l\_1}\cdot(y_1 - y_3) \tag{3}$$

The values of $\Delta\phi_{12}(\lambda_{v,l})$ and $\Delta\phi_{13}(\lambda_{v,l})$ are determined using the cross-spectrum analysis method based on Morlet wavelet analysis. As explained in Section 3.3, this method has also been utilized in Step (3) of the processing procedure for determining the initial set of SVWs. The horizontal coordinates of the profile triple, i.e., (x_1, y_1), (x_2, y_2), and (x_3, y_3), can be obtained from the latitudes and longitudes of the profiles. By solving Equations (2) and (3) simultaneously, the two parameters k_{x,l_1} and k_{y,l_1}, which are the horizontal wavenumber components of the wave signal at altitude z with a vertical wavelength of $\lambda_{v,l}$ using Profile 1 as the reference, can be obtained. The horizontal wavelength of this wave signal, λ_{h,l_1}, is then calculated using Equation (4):

$$\lambda_{h,l\_1} = \frac{2\pi}{\sqrt{k_{x,l\_1}^2 + k_{y,l\_1}^2}} \tag{4}$$

Similarly, the horizontal wavelength of the wave signal with a vertical wavelength of $\lambda_{v,l}$ using Profile 2 as the reference, λ_{h,l_2}, and that using Profile 3 as the reference, λ_{h,l_3}, are also obtained. The final horizontal wavelength $\lambda_{h,l}$ of the wave signal at altitude z with a vertical wavelength of $\lambda_{v,l}$ is calculated as (Zeng et al., 2021):

$$\lambda_{h,l} = Med(\lambda_{h,l\_1}, \lambda_{h,l\_2}, \lambda_{h,l\_3}) \tag{5}$$

where "Med" represents taking the median value. The value of $\lambda_{h,l}$ will be checked to ensure its physical validity, and the following conditions need to be satisfied (Ern et al., 2004; Preusse et al., 2006; Faber et al., 2013; Schmidt et al., 2016):

(1) $\lambda_{h,l}$ should be greater than the Nyquist wavelength, i.e., twice the maximum separation between any two profiles within the triple.

(2) $\lambda_{h,l}$ should exceed the minimum detectable horizontal wavelength for the observational technique, which is 100 km for GNSS RO technique.

(3) $\lambda_{h,l}$ should not be larger than 10,000 km. This upper limit is applied to exclude unreliable ultra-long horizontal wavelengths calculated from excessively small phase differences, which might arise from measurement noise or phase ambiguity. A $\lambda_{h,l}$ value exceeding 10,000 km is beyond the typical scales of GWs.

For each vertical wavelength in the initial set of SVWs, $\lambda_{v,l}$ ($l = 1, 2, 3, \ldots, n$), the horizontal wavelength of the corresponding wave signal, $\lambda_{h,l}$, is calculated and is checked. If any one of the above three criteria is not satisfied, $\lambda_{h,l}$ is considered invalid and the wave signal with the vertical wavelength of $\lambda_{v,l}$ is considered a non-GW signal, and $\lambda_{v,l}$ is

https://doi.org/10.5194/egusphere-2026-2400
Preprint. Discussion started: 30 April 2026

therefore removed from the set of SVWs. Otherwise, it is kept as a valid GW signal, and its MF magnitude, $MF_l(\lambda_{v,l})$, is calculated using Equation (6) (Faber et al., 2013; Schmidt et al., 2016; Zeng et al., 2021):

$$MF_l(\lambda_{v,l}) = \frac{\rho}{2}\frac{\lambda_{v,l}}{\lambda_{h,l}}\frac{g^2}{N^2}\left(\frac{\hat{T}}{\bar{T}}\right)^2 \tag{6}$$

In which, ρ represents the background atmospheric density, $\hat{T}$ denotes the temperature amplitude for the GW signal at the given altitude z with a vertical wavelength of $\lambda_{v,l}$, $\bar{T}$ represents the background temperature at this altitude, and N^2 is the squared buoyancy frequency at this altitude. $\hat{T}$ and $\bar{T}$ are extracted from the reference profile, and N^2 is calculated as follows:

$$N^2 = \frac{g}{\bar{T}}\left(\frac{\partial \bar{T}}{\partial z} + \frac{g}{c_p}\right) \tag{7}$$

where g is the gravitational acceleration, with a value of 9.80 m/s², and c_p represents the specific heat at constant pressure, with a value of 1004 J/(kg·K).

For all the wave signals with valid horizontal wavelengths, their respective MF magnitudes are obtained. Following the approach of Wright and Gille (2013), the total GW MF magnitude at altitude z, MF_{all}, is calculated by summing the MF magnitudes of all these GW signals:

$$MF_{all} = \sum_{l=1}^{k} MF_l \tag{8}$$

where k ($k \leq n$) is the number of wave signals with valid horizontal wavelengths, which is also the number of SVWs kept in the final set of SVWs. The GW signal with the largest MF magnitude is defined as the primary GW signal at the altitude z, and its MF magnitude is denoted as MF_{max}:

$$MF_{\max} = \max_{l\in\{1,2,\ldots,k\}}(MF_l) \tag{9}$$

For the temperature profile triple illustrated in Figure 1, with the threshold α set as 0.6, and at the selected altitude z = 25 km, the horizontal wavelengths of the two wave signals in the initial set of SVWs both pass the quality control. As a result, the final set of SVWs is identical to the initial one, containing two SVWs. Table 1 lists the amplitudes and the horizontal wavelengths of the two wave signals corresponding to the two SVWs, derived using different reference profiles, and the MF magnitudes of the two SVWs calculated based on their respective median horizontal wavelengths. For the wave signal shown in Figure 1(b) which is with the vertical wavelength of $\lambda_{v,1}$= 8.54 km, the median horizontal wavelength is 1669.40 km, derived with Profile 2 as the reference profile, and its MF magnitude is $MF_1 = 3.99 \times 10^{-3}$Pa. For the wave signal with the vertical wavelength of $\lambda_{v,2}$ = 12.80 km, the median horizontal wavelength is 1253.76 km, also with Profile 2 as the reference, and its MF magnitude is $MF_2 = 4.97 \times 10^{-3}$Pa. Therefore, the total GW MF magnitude at the altitude of 25 km derived from this temperature profile triple is $MF_{all} = MF_1 + MF_2 = 7.96 \times 10^{-3}$Pa. The primary wave signal is with a MF magnitude of $MF_{max} = MF_2$, accounting for 62% of the total GW MF.

https://doi.org/10.5194/egusphere-2026-2400
Preprint. Discussion started: 30 April 2026

Table 1. Wave amplitudes and horizontal wavelengths derived by using different reference profiles for the two wave signals extracted from the example triple shown in Figure 1. Values in italic fonts represent the parameters corresponding to the median horizontal wavelengths.

Vertical wavelength (km)	Reference profile index	Amplitude (K)	Horizontal wavelength (km)	Momentum flux magnitude ($10^{-3}Pa$)
	1	7.47	1670.40	
$\lambda_{v,1}$=8.54	*2*	*10.21*	*1669.40*	*3.99*
	3	6.32	1667.63	
	1	6.39	1255.46	
$\lambda_{v,2}$=12.80	*2*	*8.07*	*1253.76*	*4.97*
	3	4.42	1251.97	

4 Comparison with the Traditional Method

For the example shown in Figure 1 and Table 1, the amplitude and the MF of the wave signal $\lambda_{v,1}$ are 10.21 K and 3.99×10^{-3} Pa, respectively, and the amplitude and the MF of the wave signal $\lambda_{v,2}$ are 8.07 K and 4.97×10^{-3} Pa, respectively. This example demonstrates that wave signals with smaller amplitudes might produce larger MF, which is consistent with the conclusion of Wright and Gille (2013). With the traditional profile-triple-based method, only the wave signal with the largest amplitude (i.e., wave signal $\lambda_{v,1}$) would be considered, while the signal which actually produces larger MF (i.e., wave signal $\lambda_{v,2}$) would be overlooked. Compared with the traditional method, the new method has the advantage to provide more complete information on GW MF magnitude.

Another advantage of the new method compared with the traditional profile-triple-based method is that it is of higher data utilization. The traditional method not only requires the three profiles in the triple to meet the same spatiotemporal constraints listed in Section 3.2, but also imposes strict limitations on the differences among the vertical wavelengths of the wave signals corresponding to the maximum amplitudes respectively derived from the three profiles, which results in a very limited number of triples from which the traditional method can successfully extract GW MF. Specifically, the traditional method requires that the differences between each pair in the three vertical wavelengths corresponding to the maximum amplitudes, extracted respectively from the three temperature perturbation profiles, do not

https://doi.org/10.5194/egusphere-2026-2400
Preprint. Discussion started: 30 April 2026

exceed 2 km (the temperature profile triple shown in Figure 1(a) does satisfy this condition), and if not satisfied, it is considered that the three profiles in the triple have not detected the same GW signal, and the profile triple will be discarded (Schmidt et al., 2016).

The traditional profile-triple-based method treats GWs as monochromatic waves and estimates MF by extracting only the wave component with the maximum amplitude, i.e. the dominant signal within a complex wave field, which is effective when the wave spectrum is simple and a clearly dominant wave signal exists. While due to the diversity of GW sources (e.g., topography, convection, fronts, and jets) and processes such as nonlinear interactions, refraction, and dissipation during wave propagation, GW signals observed in practice often manifest as complex spectra resulting from the superposition of multiple GWs, rather than consisting of a single wave component (Andrews et al., 1987; Fritts and Alexander, 2003; Wright and Gille, 2013; Schmidt et al., 2016), which makes it difficult to accurately represent the multi-scale superposition characteristics of GWs in the actual atmosphere using the traditional method.

To characterize the complex GW spectral structures more objectively, following Wright and Gille (2013), we treat each vertical wavelength as an independent wave signal and attempt to extract the MF magnitudes corresponding to multiple wave components. Due to that the amplitude of a GW signal reflects its intensity (Andrews et al., 1987; Fritts and Alexander, 2003), we propose to identify SVWs by screening the HAVWRs. All wave components detected in each temperature perturbation profile of the triple are filtered based on relative amplitudes, retaining only those signals with relative amplitudes exceeding the threshold α, based on which the initial set of SVWs is identified. Although these identified wave signals may not necessarily exhibit the maximum amplitudes in some individual profiles, their relative amplitudes consistently exceed the threshold, enabling to characterize the GW structural features during actual propagation more reliably. The profile triples which are excluded by the traditional method due to that the differences among the three vertical wavelengths corresponding to the maximum amplitudes exceeding the 2 km threshold might still be useful for extracting GW MF when utilizing the new method, and Figure 2 provides such an example.

As shown in Figure 2(a), for Profile 1, the vertical wavelength of the wave signal with an amplitude of $A_{max,1}$ is 7.61 km, while for Profiles 2 and 3, the vertical wavelengths of the wave signals with amplitudes $A_{max,2}$ and $A_{max,3}$ respectively are both 12.08 km. The difference in vertical wavelength between the two wave signals of amplitudes $A_{max,1}$ and $A_{max,2}$ (or $A_{max,3}$) exceeds 2 km, and therefore this triple will be rejected if using the traditional profile-triple-based method. However, by using the new method, the HAVWRs of this profile triple are successfully identified through the procedure described in Section 3.3, which comprise two sub-ranges (r_1 and r_2). As illustrated in Figure 2(b), based on the derived HAVWRs, the initial set of SVWs is further obtained from the co-varying amplitude curves, which is $\{\lambda_{v,1} = 7.18\text{km}, \lambda_{v,2} = 7.61\text{km}, \lambda_{v,3} = 12.08\text{km}\}$. The MF magnitudes associated with these SVWs can be calculated subsequently.

Table 2 lists the amplitudes and horizontal wavelengths corresponding to all the three SVWs presented in Figure 2(b), calculated using different reference profiles. Note that the horizontal wavelength of the wave signal with a vertical wavelength of $\lambda_{v,3} = 12.08\text{km}$ exceeds 10,000 km, so this wave signal is discarded and not used for MF extraction. The

https://doi.org/10.5194/egusphere-2026-2400
Preprint. Discussion started: 30 April 2026

final set of SVWs is $\{\lambda_{v,1} = 7.18\text{km}, \lambda_{v,2} = 7.61\text{km}\}$, and the MF magnitudes of the two wave signals in the set are $MF_1 = 6.66 \times 10^{-2}$Pa and $MF_2 = 7.23 \times 10^{-2}$Pa, respectively. MF_2 is larger than MF_1, so the wave signal corresponding to $\lambda_{v,2}$ is the dominant wave signal, i.e., $MF_{max} = MF_2$. The total GW MF magnitude is $MF_{all} = MF_1 + MF_2 = 13.89 \times 10^{-2}$Pa, of which the contribution of the dominant wave signal accounts for 52%.

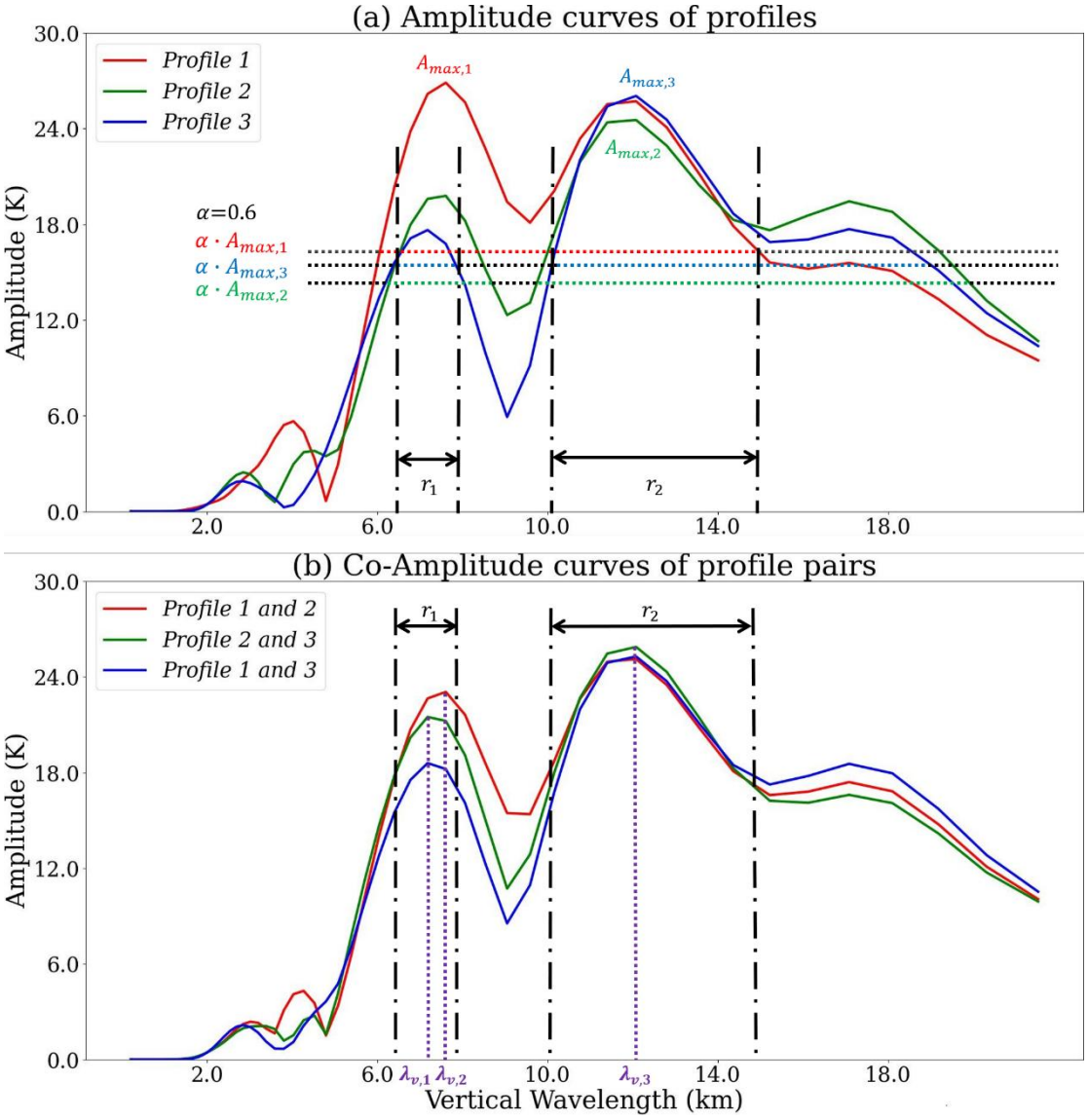

Figure 2: Similar to Figure 1, while using a profile triple of Type B.

https://doi.org/10.5194/egusphere-2026-2400
Preprint. Discussion started: 30 April 2026

Table 2. Wave amplitudes and horizontal wavelengths derived by using different reference profiles for the two wave signals extracted from the example triple shown in Figure 2. Values in italic fonts represent the parameters corresponding to the median horizontal wavelengths.

Vertical wavelength (km)	Reference profile index	Amplitude (K)	Horizontal wavelength (km)	Momentum flux magnitude ($10^{-3}Pa$)
	1	26.18	3067.71	
$\lambda_{v,1}$=7.18	*2*	*19.60*	*3045.78*	*6.66*
	3	17.65	3042.27	
	1	26.88	3052.55	
$\lambda_{v,2}$=7.61	*2*	*19.79*	*3030.54*	*7.23*
	3	16.78	3026.51	
	1	25.72	18557.72	
$\lambda_{v,3}$=12.08	2	24.55	18476.64	
	3	*26.06*	*18497.40*	

For the convenience of comparison and discussion, triples similar to the one shown in Figure 1 and Table 1 are designated as Type A triples, and those similar to the one shown in Figure 2 and Table 2 are referred to as Type B triples. For Type A triples, the condition that the pairwise differences among the vertical wavelengths corresponding to the maximum-amplitude wave signals extracted respectively from the three profiles are all no larger than 2 km is satisfied, and both the new method and the traditional method can successfully extract MF magnitudes from these triples. For Type B triples, the condition is not satisfied, and such triples are therefore discarded by the traditional method, while with the new method, the SVWs can be obtained and the MF magnitudes of the corresponding GW signals can still be derived successfully from these triples. The new method improves the utilization rate of profile triples for the retrieving of GW MF magnitudes by effectively utilizing Type B triples. To quantify the contributions of the two types of triples to the derived GW magnitudes, the GW MF extracted from Type A and Type B triples will be further compared statistically in Section 5.4.

Note that we define the primary wave signal as the wave signal yielding the maximum MF magnitude, rather than the one with the largest amplitude. This is due to that for the waves with different vertical wavelengths in the set of SVWs, the reference profiles selected for calculating their MF magnitudes, i.e., the profiles corresponding to the median horizontal

https://doi.org/10.5194/egusphere-2026-2400
Preprint. Discussion started: 30 April 2026

wavelengths, might be different. Taking the profile triple shown in Figure 2 and Table 2 for example, Profile 2 is selected as the reference profile when calculating the MF magnitude for the wave signal with a vertical wavelength of $\lambda_{v,2}$, whereas for the wave signal with a vertical wavelength of $\lambda_{v,3}$, Profile 3 is selected as the final reference profile. For different wave signals within the set of SVWs, when the selected reference profiles for calculating their MF magnitudes are different, to determine their relative strength by comparing their amplitudes is physically questionable. Therefore, the primary wave signal is identified based on MF magnitude of the signal in the new method.

5 Results and Discussion

5.1 Determination of the Empirical Threshold α

In the new method, the value of the empirical threshold α influences the determination of the HAVWRs, which subsequently affects the final set of SVWs, as well as the calculated MF_{all} and MF_{max}. This section discusses the strategy for selecting α based on the zonal averaged GW MF magnitudes retrieved utilizing different α. MF_{all} and MF_{max} are derived from each qualified profile triple, and their zonal averages, denoted as $\overline{MF_{all}}$ and $\overline{MF_{max}}$, are defined as follows:

Within the 40°S–40°N latitude range, which is covered by COSMIC-2 RO observations, central latitudes are selected at 5° intervals, and there are 17 central latitudes (including 40°N and 40°S) in total. At a given central latitude, the corresponding zonal average of MF_{all} (MF_{max}), i.e., $\overline{MF_{all}}$ ($\overline{MF_{max}}$), is calculated as the average value of MF_{all} (MF_{max}) derived from all qualified profile triples located within the corresponding ±5° latitude band centered at that latitude. Note that latitude bands corresponding to adjacent central latitudes partially overlap, and that the geographic location of each triple is determined by averaging the longitudes and latitudes of its three constituent profiles.

For comparison, MF magnitudes are also derived by using the traditional profile-triple-based method, and their zonal averages are calculated following similar procedure. As described in Section 4, the traditional method extracts the MF of the highest-amplitude wavelike signals (abbreviated as HAWS), and so the corresponding MF magnitude derived from a single profile triple and the zonal averaged MF magnitude are respectively denoted as MF_{HAWS} and $\overline{MF_{HAWS}}$.

5.1.1 $\overline{MF_{all}}$ and $\overline{MF_{max}}$ Obtained with Different α Values

Figure 3 displays the variations of $\overline{MF_{max}}$ (dashed lines) and $\overline{MF_{all}}$ (solid lines) over the latitude range of 40°S–40°N at the altitude level of 25 km, derived with the new method from COSMIC-2 dry temperature profile triples during June–August 2020, while utilizing different α values. For comparison, Figure 3 also presents the variations of $\overline{MF_{HAWS}}$, which is calculated using the traditional profile-triple-based method. Both $\overline{MF_{HAWS}}$ and $\overline{MF_{max}}$ obtained using different α values exhibit peaks near the equator, reaching approximately 0.15 Pa. All the three zonal averaged values, $\overline{MF_{HAWS}}$, $\overline{MF_{max}}$, and $\overline{MF_{all}}$, are generally slightly higher in the 0°–20°N latitude band than in the 0°–20°S band, consistent with previous studies which report that GW MF magnitudes peak in the low-latitudes of the NH (Alexander et al., 2008; Ern et al., 2011; Faber et

https://doi.org/10.5194/egusphere-2026-2400
Preprint. Discussion started: 30 April 2026

al., 2013; Geller et al., 2013; Wright and Gille, 2013; Alexander, 2015; Zeng et al., 2021). As α decreases from 0.9 to 0.3, the peak of $\overline{MF_{all}}$ gradually shifts northward from near the equator to around 15°N, indicating the presence of more potential GW signals in the low-latitudes of the NH which are difficult to detect using the traditional method, consistent with Wright and Gille (2013).

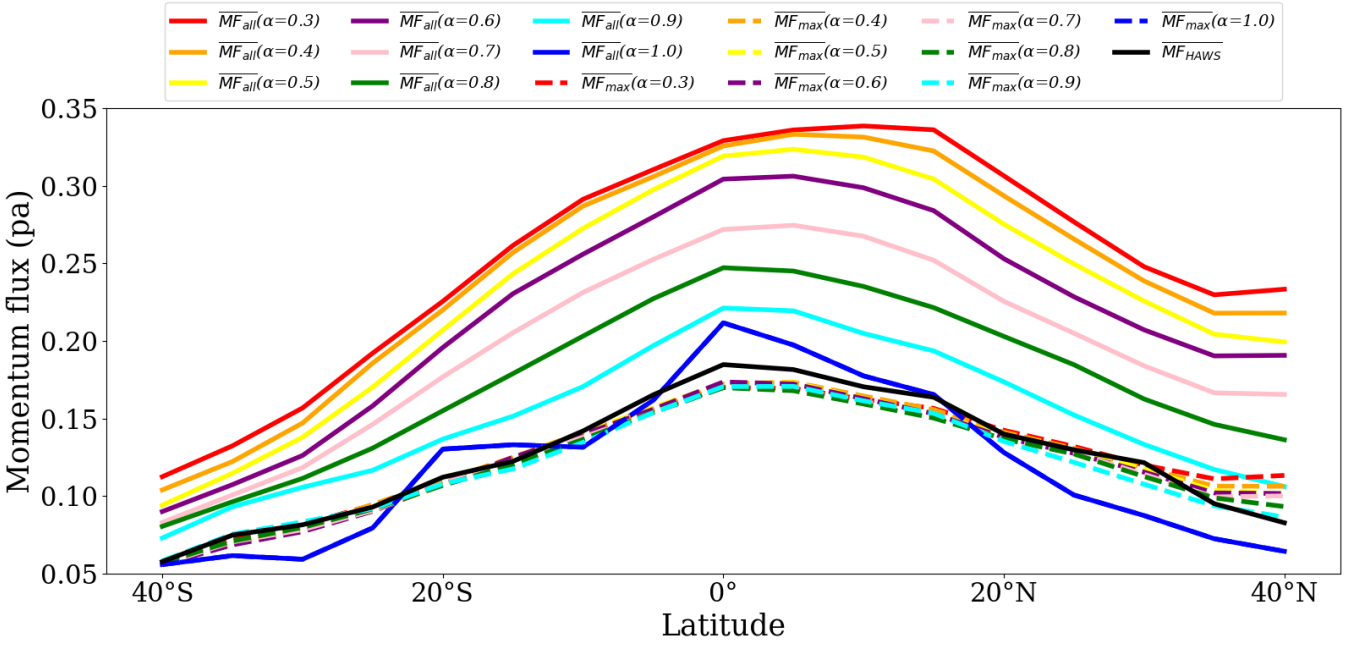

Figure 3: Variations of the zonal averaged momentum flux magnitudes at 25 km: $\overline{MF_{HAWS}}$, and $\overline{MF_{max}}$ and $\overline{MF_{all}}$ calculated using different α values.

Table 3 lists the numbers of qualified profile triples from which GW MF magnitudes are successfully retrieved by the traditional profile-triple-based method and by the new method when using different α values between 0.3 and 1.0, in steps of $\Delta\alpha = 0.1$. When using the new method, the number of qualified triples increases when α decreases, which can be explained as follows. For any given profile triple, the vertical wavelengths corresponding to the local maxima on the co-varying amplitude curves (obtained from cross-spectral analysis of the profile pairs within the triple) remain fixed. As α decreases, the HAVWRs generally expand. A profile triple is classified as qualified as long as the HAVWRs cover the vertical wavelengths corresponding to the local maximum co-varying amplitudes, and a smaller α allows more triples to meet the qualification criteria, leading to an increase in the number of qualified triples. Table 3 also shows that with the traditional profile-triple-based method, GW MF magnitudes can be successfully retrieved from only 3,785 qualified triples, while when using the new method, the number of qualified triples reaches 5,560 when $\alpha = 0.9$, and when α decreases to 0.8, the number of qualified triples reaches 7,922, which is larger than twice as many qualified triples as the traditional method. These results demonstrate the advantage of the new method in terms of data utilization.

https://doi.org/10.5194/egusphere-2026-2400
Preprint. Discussion started: 30 April 2026

Note that when α = 1.0, the number of qualified triples is very limited, which is attributed to two factors. First, when α = 1.0, the initial set of SVWs for a triple exists only when the vertical wavelengths corresponding to the maximum-amplitude wave signals of all the three profiles, i.e., $A_{max,i}$ (i=1,2, and 3), are completely identical, which is a very strict condition. For the triple shown in Figure 1, when α = 1.0, all three profiles in this triple exhibit the maximum amplitudes at the same vertical wavelength of $\lambda_{v,1} = 8.54$ km, and the initial set of SVWs can be determined, which is SVWs $= \{\lambda_{v,1}\}$. While for the triple illustrated in Figure 2, when α = 1.0, the maximum-amplitude wave signal of Profile 1 has a vertical wavelength of $\lambda_{v,2}$ =7.61 km, and the maximum-amplitude wave signals of Profiles 2 and 3 both have a vertical wavelength of $\lambda_{v,3}$ =12.08 km. The HAVWR of each profile includes only the vertical wavelength corresponding to its amplitude peak, and therefore the intersection of the HAVWRs of all the three amplitude curves is an empty set. Consequently, this triple fails to determine the initial set of SVWs and is therefore discarded. Second, as explained in Section 3.4, even for the triples from which the initial set of SVWs can be successfully identified, the horizontal wavelength of the wave signal corresponding to a SVW must satisfy additional criteria to be considered valid. Due to these two factors, when α is set as 1.0, a large number of triples are discarded, resulting in a very limited number of valid triples.

Table 3. Number of qualified triples obtained by the traditional profile-triple-based method and by the newly proposed method when using different α values.

Method	α	Number of qualified profile triples
Traditional method	/	3,785
Proposed method	0.3	11,667
	0.4	11,306
	0.5	10,937
	0.6	10,308
	0.7	9,379
	0.8	7,922
	0.9	5,560
	1.0	690

https://doi.org/10.5194/egusphere-2026-2400
Preprint. Discussion started: 30 April 2026

To facilitate a more intuitive comparison between the new method and the traditional profile-triple-based method, we define the parameter $Ratio = \overline{MF_{all}}/\overline{MF_{HAWS}}$. Figure 4 illustrates the latitudinal distributions of Ratio values at the altitude of 25 km when using different α values. Within the 40°S–40°N latitude range, with different settings of α, the peak values of Ratio are generally obtained near 40°N, which should be attributed to two factors. First, the 40°N zone is a region of relatively weak GW activity. As revealed by Figure 3, at around 40°N, both $\overline{MF_{all}}$ and $\overline{MF_{HAWS}}$ generally reach the minima of the NH across various α values, and $\overline{MF_{HAWS}}$ is even lower than $\overline{MF_{max}}$ for most α settings. Second, the exceptionally low background MF ($\overline{MF_{HAWS}}$) serves as the denominator for the calculation of Ratio, thereby resulting in its peak value where GW activity is relatively weak.

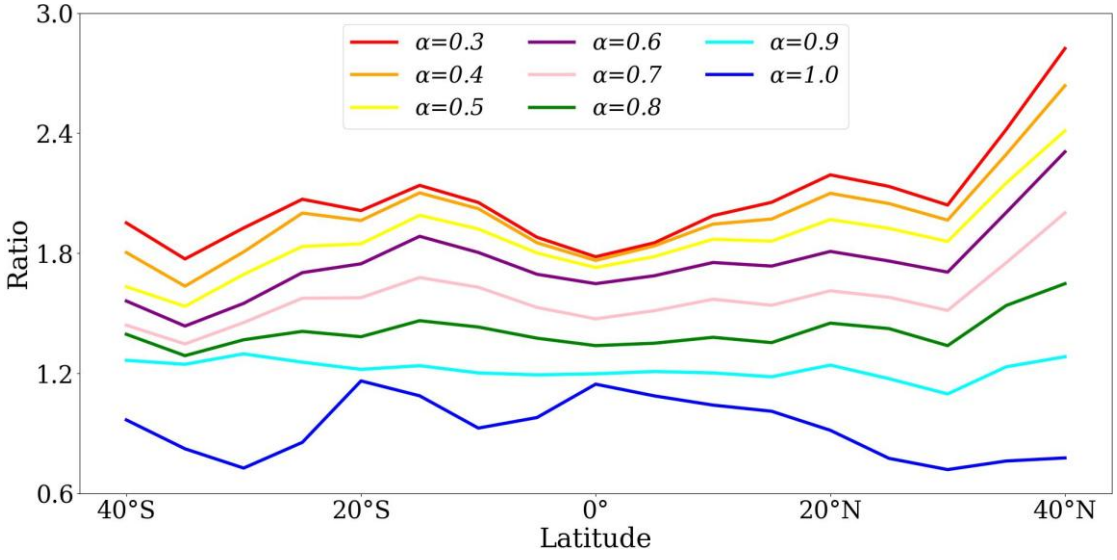

Figure 4: Latitudinal distributions of Ratio values at 25 km with different settings of α.

With different settings of α, secondary peaks in Ratio are observed in the low-latitudes of both hemispheres, near 15°S and 20°N. The region near 20°N features complex topography, frequent monsoonal and convective activity, and significant background wind variations (Holton, 1983; Alexander et al., 1995; Alexander and Vincent, 2000; Fritts and Alexander, 2003; Hei et al., 2008). These factors collectively make this zone highly active in terms of multiple GW sources, and a typical example is the Indian subcontinent and its surrounding areas (Ratnam et al., 2008; Wright and Gille, 2011; Vincent and Alexander, 2000; Rakshit et al., 2018; Jana et al., 2020; Hou et al., 2024). GW signals detected by COSMIC-2 RO data are likely the superposition of waves originating from different sources, and in the extracted temperature amplitude curves, multiple peaks across the vertical wavelength range may correspond to individual monochromatic GWs from distinct sources. Our results are highly consistent with Wright and Gille (2013) in that over the tropical region north of the equator, the total MF magnitude of all GW signals is nearly twice that of the largest-amplitude wave signal alone. Although $\overline{MF_{HAWS}}$,

https://doi.org/10.5194/egusphere-2026-2400
Preprint. Discussion started: 30 April 2026

which considers only the contribution of the highest-amplitude GW signal, is also generally large in the NH low latitudes, the contribution from non-dominant-amplitude GWs captured by our method significantly enhances $\overline{MF_{all}}$, leading to the secondary peak in Ratio. Our method has the advantage of capturing GW signals and their MF contributions which are often ignored by traditional approaches, thereby providing a more comprehensive estimation of GW MF magnitude.

Previous studies have also documented the presence of multiple GW sources in the Southern Hemisphere (SH) low latitudes (near 15°S). Hocke and Tsuda (2001) identified multiple regions of enhanced stratospheric GW activity associated with tropical convection zones in the SH, located over Brazil, Africa, Indonesia/Australia, and the Pacific Ocean. Ayorinde et al. (2023) also found that convective activity is the primary driver of GWs in the tropical region of South America. Furthermore, multiple studies have confirmed that the Andes Mountains, which run along the western coast of South America, serve as a hotspot for the excitation of orographic GWs (Alexander et al., 2015; Hindley et al., 2015; Ayorinde et al., 2023). The presence of these multiple GW sources may lead to that $\overline{MF_{all}}$ is significantly larger than $\overline{MF_{HAWS}}$ within the low-latitude band of the SH, which explains the appearance of the secondary Ratio peak near 15°S in Figure 4.

Figures 3 and 4 show that when $\alpha < 1.0$, $\overline{MF_{all}}$ is generally higher than $\overline{MF_{HAWS}}$ and it gradually increases as α decreases, which leads to the monotonic increase of Ratio with α. This is because that a lower α value broadens the HAVWRs, increasing the number of initial SVWs identified within a single profile triple, which in turn leads to an increase in the retrieved MF_{all}, ultimately leading to an increase in the calculated zonal mean MF magnitude, $\overline{MF_{all}}$.

Different α values not only cause the variations in the HAVWRs and the initial SVWs, but also cause the variations in the number of qualified profile triples, which also contribute to the α-dependent variations of $\overline{MF_{all}}$ presented in Figure 3. To further elucidate only the influence of the variations in HAVWRs and initial SVWs, we perform MF retrievals using a fixed set of profile triples across different α values. Specifically, the triple set $S_{\alpha=0.9}$ is defined, comprising the 5,560 qualified triples from which MF magnitudes can be successfully retrieved when $\alpha = 0.9$ (refer to Table 3). Based on this triple set, the zonal variations of $\overline{MF_{max}}$ and $\overline{MF_{all}}$ at the altitude level of 25 km are obtained, by setting α as 0.3, 0.6, and 0.9, respectively, and the results are shown in Figure 5. In this scenario, for different α, the variations of $\overline{MF_{all}}$ and $\overline{MF_{max}}$ are purely caused by the variations in the HAVWRs and the initial SVWs. Both $\overline{MF_{max}}$ and $\overline{MF_{all}}$ increase significantly as α decreases. This is due to that when α decreases, both the HAVWRs and the initial set of SVWs expand, and if a vertical wavelength newly added in the initial set of SVWs corresponds to a wave signal with larger MF than that of the original dominant wave in the set, it will be identified as the new dominant wave. Therefore, for a given triple, the MF_{max} retrieved with a smaller α is always no less than that obtained with a larger α, and consequently, based on the same triple set, the zonal averaged value of MF_{max}, i.e. $\overline{MF_{max}}$, gradually increases as α decreases. Similarly, the decrease in α also leads to the increase in the number of SVWs, the corresponding increases in MF_{all} and $\overline{MF_{all}}$.

https://doi.org/10.5194/egusphere-2026-2400
Preprint. Discussion started: 30 April 2026

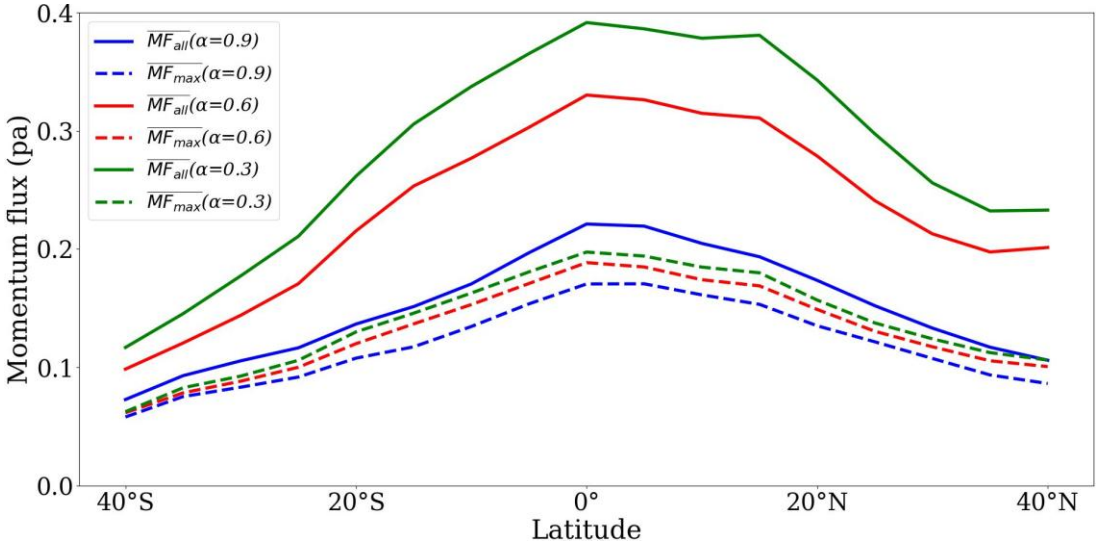

Figure 5: Zonal averaged momentum flux magnitudes ($\overline{MF_{max}}$ and $\overline{MF_{all}}$) at 25 km derived based on the triple set $S_{\alpha=0.9}$, by setting α as 0.3, 0.6, and 0.9, respectively.

5.1.2 The Effect of an Undersized α Values

As already explained, for a given triple, a decrease in α value leads to increases in the retrieved MF_{max} and MF_{all}. However, an excessively small α value might lead to incorporating the vertical wavelengths of spurious low-amplitude local maximum wave signals, as exemplified by the minor wave peaks within the 4–6 km vertical wavelength range shown in Figure 1, in the initial set of SVWs. According to Equation (6), the MF magnitude derived from a single wave signal is proportional to the square of its temperature amplitude. Therefore, when using a small α value, if a given triple can only identify SVWs corresponding to low-amplitude wave signals, the MF_{max} and MF_{all} derived from it will be typically lower than those derived from triples that are of SVWs corresponding to high-amplitude wave signals. To exemplify the effect of an undersized α value, the triple sets $S_{\alpha=0.3}$ and $S_{\alpha=0.6}$ are defined, which respectively comprise the 11,667 valid triples for α=0.3 and the 10,308 valid triples for α=0.6 (refer to Table 3), and apparently, $S_{\alpha=0.3} \supset S_{\alpha=0.6}$. The set difference between $S_{\alpha=0.3}$ and $S_{\alpha=0.6}$ is defined as the triple set S'. With the method introduced in Section 3, the SVWs extracted for the triples in set S' generally correspond to wave signals with lower amplitudes compared to those extracted for the triples in set $S_{\alpha=0.6}$. Figure 6 displays the variations of $\overline{MF_{max}}$ and $\overline{MF_{all}}$ at the 25 km altitude level, derived respectively from the three triple sets, all by setting $\alpha = 0.3$. With the same α value, $\overline{MF_{max}}$ and $\overline{MF_{all}}$ derived from the set S' are significantly lower than those from the set $S_{\alpha=0.6}$, which is because that the MF magnitudes of the lower-amplitude wave signals extracted from the set S' are inherently much smaller than those of the higher-amplitude wave signals extracted from the set $S_{\alpha=0.6}$. Moreover, the smaller MF obtained from the triple set S' lowers the zonal averages of MF_{max} and MF_{all}, making $\overline{MF_{max}}$ and $\overline{MF_{all}}$ obtained from $S_{\alpha=0.3}$ generally smaller than those from $S_{\alpha=0.6}$.

https://doi.org/10.5194/egusphere-2026-2400
Preprint. Discussion started: 30 April 2026

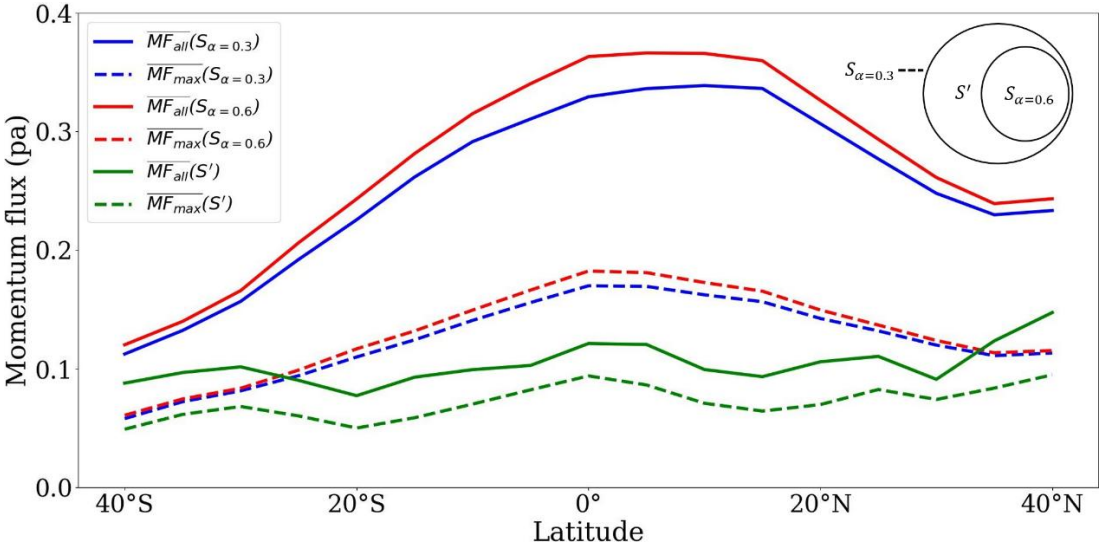

Figure 6: $\overline{MF_{max}}$ and $\overline{MF_{all}}$ at 25 km calculated respectively from the triple sets $S_{\alpha=0.3}$, $S_{\alpha=0.6}$, and S', all by setting α as 0.3.

5.1.3 Optimal Selection of the Parameter α

The discussions in Sections 5.1.1 and 5.1.2 explain why the decrease of α leads to the increase in the retrieved $\overline{MF_{all}}$ and $\overline{MF_{max}}$ and demonstrate that an undersized α value would lead to incorporating the contribution of low-amplitude wave signals into the results. The low-amplitude local maximum wave signals extracted when α is set to an undersized value may represent pseudo-GW signals arising from instrumental noise or detrending errors. Fritts and Alexander (2003) emphasized that although the GW field is theoretically composed of multi-scale wave components, its spectral structure is often dominated by one or a few large-amplitude wave modes. Ern et al. (2004) noted that instrumental noise and detrending errors can produce spurious signals that may be misinterpreted as GWs. In their experiments, an amplitude threshold was applied to filter out such non-physical contributions. When applying our new method, to minimize the potential influence of lower-amplitude local maximum wave signals on the results, a robust methodology for selecting the optimal α is needed.

Figures 3 and 4 indicate that when α decreases below a certain threshold, its effect on enhancing $\overline{MF_{all}}$ diminishes significantly. As shown in Figure 3, the mean difference between the $\overline{MF_{all}}$ curves corresponding to α= 0.3 and α= 0.4 is significantly smaller than that between the $\overline{MF_{all}}$ curves corresponding to α= 0.6 and α= 0.7. To quantify the mean difference in $\overline{MF_{all}}$ obtained when using two different settings of α, the following two statistical parameters are defined:

$$MeanDiff\,(\alpha_1,\alpha_2)=\sum_{i=1}^{N}\left[\overline{MF_{all}}(\alpha_1,i)-\overline{MF_{all}}(\alpha_2,i)\right] \tag{10}$$

$$D(\alpha,\Delta\alpha)=MeanDiff\,(\alpha,\alpha+\Delta\alpha)-MeanDiff\,(\alpha-\Delta\alpha,\alpha) \tag{11}$$

https://doi.org/10.5194/egusphere-2026-2400
Preprint. Discussion started: 30 April 2026

In Equation (10), $\overline{MF_{all}}(\alpha, i)$ denotes the value of $\overline{MF_{all}}$ at the i-th ($i = 1,2, \ldots, N$) central latitude corresponding to a given α. N is the total number of central latitude values and N=17. The parameter $\mathrm{MeanDiff}(\alpha_1, \alpha_2)$ quantifies the overall mean difference between the two $\overline{MF_{all}}$ curves, which respectively corresponds to α=α_1 and α=α_2, across all central latitudes between 40°S–40°N. The parameter $D(\alpha, \Delta\alpha)$, defined by Equation (11), measures the asymmetry in MeanDiff as α changes with a step size of $\Delta\alpha$. As explained in Section 5.1.1, $\Delta\alpha$ is set as 0.1 in the present study.

Since $\overline{MF_{all}}$ generally increases as α decreases, for a given step size $\Delta\alpha$ ($\Delta\alpha > 0$), a pronounced peak in $D(\alpha, \Delta\alpha)$ occurring at $\alpha = \alpha_0$ indicates that the average increase in $\overline{MF_{all}}$ associated with a decrease in α from α_0 to $\alpha_0 - \Delta\alpha$ is significantly smaller than that associated with a decrease in α from $\alpha_0 + \Delta\alpha$ to α_0. This signifies a key shift in the growth rate of the mean value of $\overline{MF_{all}}$ with respect to α at around α_0, identifying α_0 as a critical threshold. Once α falls below α_0, further decrease in α would not lead to significant enhancement in the mean value of $\overline{MF_{all}}$, indicating that the total MF magnitude is approaching saturation. Actually, when α decreases from α_0 to $\alpha_0 - \Delta\alpha$, the newly qualified triples and the newly identified SVWs within existing triples predominantly correspond to wave signals with relatively low amplitudes. These wave signals, which contribute only marginally to the total MF derived, may include components originating from instrumental noise or artifacts introduced during data processing, rather than representing physically realistic GW signals. Therefore, the diminished enhancement in the MF derived when α falls below the critical threshold α_0 can be attributed to the limited contribution of the newly introduced low-amplitude local maximum wave signals to the total MF. This in turn indicates that GW signals dominating the MF have been sufficiently captured when $\alpha = \alpha_0$, and that further decrease in α would only increase the possibility of including spurious GW signals caused by instrumental noise and detrending errors. To reach a balance between the completeness of MF information and the reliability of GW signals considered, the optimal value of α should be the one corresponding to the maximum of $D(\alpha, \Delta\alpha)$.

When α = 1.0, the number of qualified profile triples is very limited (only 690 sets), so the $\overline{MF_{all}}$ derived is of low reliability. According to Equations (10) and (11), calculating $D(\alpha, \Delta\alpha)$ requires the use of $\overline{MF_{all}}$ curves corresponding to both $\alpha + \Delta\alpha$ and $\alpha - \Delta\alpha$. The low reliability of $\overline{MF_{all}}$ corresponding to α =1.0 would also affect the reliability of the computed $D(0.9,0.1)$. Therefore, both 1.0 and 0.9 are excluded from the candidates for the optimal α value. The values of $D(\alpha, 0.1)$ corresponding to the α values of 0.4, 0.5, 0.6, 0.7, and 0.8 are respectively derived and are presented in Table 4. $D(0.7,0.1)$ is a negative value, implying that the enhancement in $\overline{MF_{all}}$ resulting from newly qualified triples and newly identified SVWs obtained when α decreases from 0.7 to 0.6 is greater than that obtained when α decreases from 0.8 to 0.7. $D(\alpha, 0.1)$ reaches the maximum when $\alpha = 0.6$, demonstrating that the increase in $\overline{MF_{all}}$ obtained when α decreases from 0.6 to 0.5 is significantly smaller than that obtained when α decreases from 0.7 to 0.6, implying the inclusion of newly captured GW signals carrying substantial MF while α decreases from 0.7 to 0.6. Table 4 demonstrates that α = 0.6 represents an optimal balance: above this threshold, the newly proposed method captures only a limited number of GW signals carrying significant MF, while below it, the incremental gain in MF is mainly attributed to the wave signals with relatively small

https://doi.org/10.5194/egusphere-2026-2400
Preprint. Discussion started: 30 April 2026

amplitudes, which increases the likelihood of including spurious signals caused by noise and detrending errors. So, in the subsequent experiments of the present study, the optimal value of α is set as 0.6.

Table 4. Values of $D(\alpha, \Delta\alpha)$ for different α values ($\Delta\alpha = 0.1$).

α	$D(\alpha, 0.1)(10^{-3}\text{Pa})$
0.4	4.53
0.5	1.91
0.6	7.62
0.7	-1.07
0.8	2.21

Note that the above strategy for determining the optimal parameter α is based on discrete sampling of α. Theoretically, reducing $\Delta\alpha$ would allow the obtained optimal α to more closely approximate the theoretical optimum. However, calculating $D(\alpha, \Delta\alpha)$ requires obtaining $\overline{MF_{all}}$ values for α, $\alpha + \Delta\alpha$, and $\alpha - \Delta\alpha$. A smaller step size $\Delta\alpha$ would substantially increase the computational burden. Considering both computational efficiency and the main objectives of the present study, $\Delta\alpha$ is set to 0.1 in this work. In our future work, we will utilize machine learning methods to enable efficient and automated searching for the optimal α value, thereby overcoming the limitations of the current discrete sampling approach.

5.2 $\overline{MF_{all}}$ and $\overline{MF_{max}}$ at Different Altitude Levels

Figure 7 presents the variations of $\overline{MF_{all}}$ and $\overline{MF_{max}}$, along with the Ratio of $\overline{MF_{max}}/\overline{MF_{all}}$, as functions of latitude at the four altitude levels of 20 km, 25 km, 30 km, and 35 km, within the latitudes of 40°S–40°N during June–August 2020, with α set as 0.6. At all the four altitude levels, the maximum values of $\overline{MF_{all}}$ and $\overline{MF_{max}}$ consistently occur in the low-latitudes of the NH, which aligns with the findings reported by Ern et al. (2011). Using data observed from the Cryogenic Infrared Spectrometers and Telescopes for the Atmosphere-2 (CRISTA-2) during August 1997, High Resolution Dynamics Limb Sounder (HIRDLS) and Sounding of the Atmosphere using Broadband Emission Radiometry (SABER) in August 2006, Ern et al. (2011) calculated the GW MF magnitude and found that the mean MF values at 25–45 km across all latitude bands (including 40°S–40°N) decrease with height, with a pronounced peak near 20°N.

https://doi.org/10.5194/egusphere-2026-2400
Preprint. Discussion started: 30 April 2026

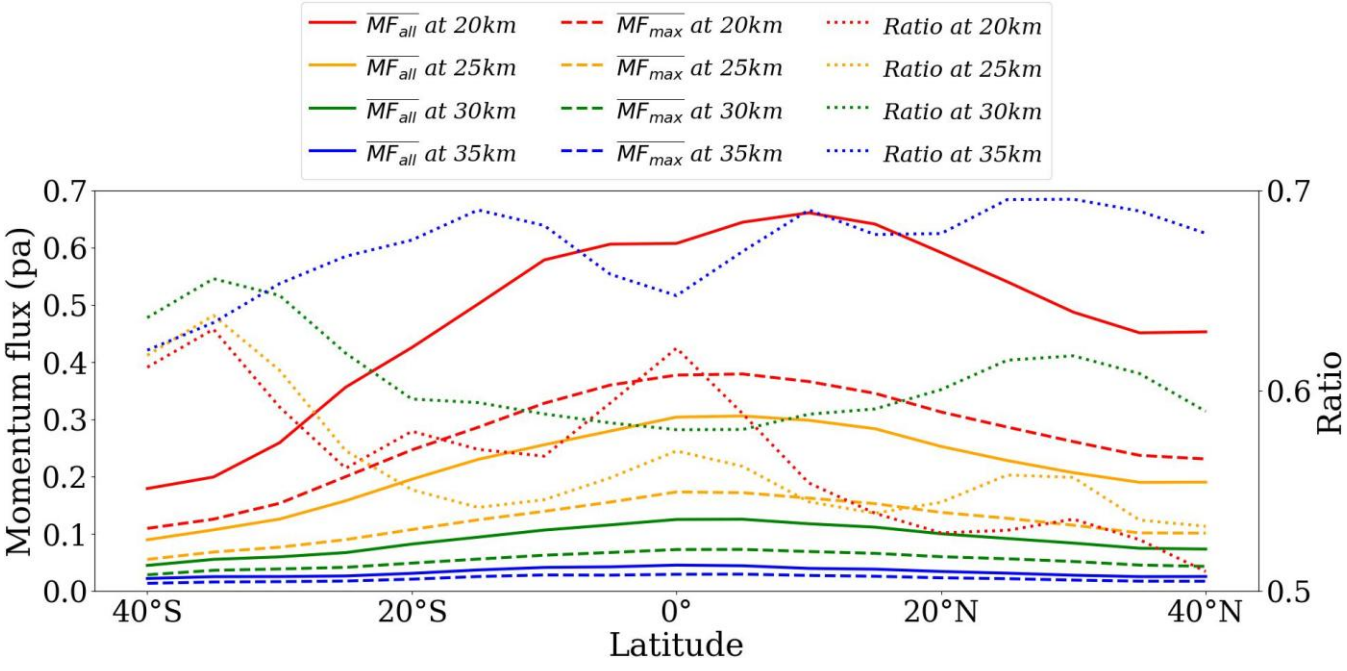

Figure 7: Latitudinal variations of $\overline{MF_{all}}$, $\overline{MF_{max}}$, and Ratio (referring to the right vertical axis) at different altitude levels, by setting α as 0.6.

Figure 7 shows that both $\overline{MF_{all}}$ and $\overline{MF_{max}}$ generally decrease with increasing altitude. The attenuation of GW MF magnitude with increasing altitude in the lower stratosphere is primarily attributed to the concentration of GW sources near or below the tropopause, with few sources existing within the stratosphere. As GWs propagate upward, they gradually weaken due to energy dissipation, leading to a corresponding decrease in the transported MF. This dissipation arises from various atmospheric processes, including radiative damping, wave–wave and wave–mean flow interactions, as well as wave breaking and instability mechanisms (Fels, 1984; Broutman and Grimshaw, 1988; Zhu, 1994; Sutherland, 2000, 2001; Fritts and Alexander, 2003). When propagating upward from the wave sources, the magnitudes of GW MF generally grow exponentially with height. When waves reach the wave breaking height levels, which are generally below 30 km, the combined effect of the waves and the background fields can cause the total temperature lapse rate to exceed the dry adiabatic lapse rate, triggering convective instability and leading to wave breaking. Above this level, GWs enter a saturated state, and increasing eddy diffusion acts to maintain atmospheric neutral stability, ultimately resulting in wave fragmentation. These physical processes collectively lead to a marked decline in GW MF with height in the lower stratosphere (Lindzen, 1981; Fritts and Alexander, 2003).

Figure 7 also demonstrates that the values of Ratio at all four altitude levels vary within the range of 0.5–0.7, and are generally lower at 20 km and 25 km than at 30 km and 35 km. This may be attributed to the fact that the gradual breaking of upward-propagating GWs near the tropopause and in the lower stratosphere (approximately 20–25 km) produces multiple

https://doi.org/10.5194/egusphere-2026-2400
Preprint. Discussion started: 30 April 2026

secondary GWs or turbulent signals, and therefore the number of non-primary GW signals detected increases, leading to a relatively smaller contribution of the primary wave to the total MF at 20 km and 25 km. Both original and secondary GW signals experience increased dissipation, and only a limited number of robust signals persist and contribute significantly to the MF at higher altitudes. Consequently, both $\overline{MF_{all}}$ and $\overline{MF_{max}}$ decrease with height above 25 km, while the Ratio of $\overline{MF_{max}}/\overline{MF_{all}}$ gradually increases at the altitudes of 30 km and 35 km. Further investigations on GW breaking phenomena in the lower stratosphere will be conducted based on the newly proposed method in our future work.

5.3 Momentum Flux from Different Types of Triples

As explained in Sections 4 and 5.1, the MF_{HAWS} retrieved by the traditional profile-triple-based method is solely from the contribution of the largest-amplitude GW signal, whereas the MF_{all} retrieved by the new method represents the collective contributions of all GW signals in the final set of SVWs. Note that the MF_{max} derived by the new method corresponds to the wave signal with the largest MF magnitude, not necessarily being the one with the largest amplitude. As stated in Section 4, the traditional method only utilizes Type A triples for GW MF retrieval, while the new method enables MF calculation from both Type A and Type B triples. In this section, the contributions of the two different types of triples to the GW MF magnitudes retrieved by the proposed method, together with the GW MF retrieved by the traditional method, are compared.

5.3.1 Comparison of the Numbers of Different Types of Triples

Table 5 presents the statistics on the numbers of different types of triples successfully used for MF retrieval using the new method (with α = 0.6) and using the traditional profile-triple-based method. With the newly proposed method, the numbers of valid Type A and Type B temperature profile triples are 4,760 and 5,548, respectively, resulting in a total of 10,308 valid triples, consistent with the information shown in Table 3. In contrast, when applying the traditional profile-triple-based method, the number of qualified profile triples that successfully yield MF_{HAWS} is only 3,785.

Table 5. Statistics on the numbers of qualified triples by using the new and the traditional methods.

Method	Triple type	Number of triples
Traditional method	A	3,785
Proposed method	A	4,760
	B	5,548
	Total	10,308

https://doi.org/10.5194/egusphere-2026-2400
Preprint. Discussion started: 30 April 2026

Table 5 reveals that even when only using Type A triples, which satisfy that the pairwise differences among the three vertical wavelengths corresponding to the maximum-amplitude wave signals extracted respectively from the three temperature perturbation profiles do not exceed 2 km, a discrepancy still exists in the numbers of final qualified triples between the traditional and the new methods. This is due to the fact that in the traditional method, MF_{HAWS} is calculated for each individual triple based solely on the maximum-amplitude wave signal, and if the GW parameters retrieved from this wave signal fail to satisfy the quality control criteria (such as constraints on the retrieved horizontal wavelength), the triple will be discarded. In contrast, the new method retrieves MF based on a set of SVWs. If the GW parameters retrieved from the wave signal corresponding to the primary-peak amplitude fail to satisfy the constraint criteria, valid MF might still be obtained if the GW parameters retrieved from other wave signals in the set of SVWs meet the constraints.

5.3.2 Comparison of the Zonal Averaged Momentum Flux from Different Types of Triples

For the convenience of discussion, the total (the largest) GW MF retrieved from individual Type A and Type B qualified triples using the new method are respectively denoted as $MF_{all\_}A$ and $MF_{all\_}B$ ($MF_{max\_}A$ and $MF_{max\_}B$), with the corresponding zonal averaged values represented as $\overline{MF_{all\_}A}$ and $\overline{MF_{all\_}B}$ ($\overline{MF_{max\_}A}$ and $\overline{MF_{max\_}B}$). Figure 8 displays the latitudinal variations of $\overline{MF_{all\_}A}$, $\overline{MF_{all\_}B}$, $\overline{MF_{max\_}A}$ and $\overline{MF_{max\_}B}$ at the height of 25 km, based on COSMIC–2 dry temperature profiles during June–August, 2020, with α = 0.6. Also shown are the latitudinal variations of $\overline{MF_{all}}$ and $\overline{MF_{max}}$, which are obtained from all qualified triples, as well as the variation of $\overline{MF_{HAWS}}$, retrieved using the traditional profile-triple-based method.

Figure 8 shows that the overall difference between $\overline{MF_{max\_}A}$ and $\overline{MF_{HAWS}}$ is relatively small, with the mean absolute difference across all latitudes between 40°S–40°N of only 2.84×10^{-3}Pa. Their difference within the tropical region of 10°S–5°N is negligible, and the maximum difference of about 11.03×10^{-3}Pa occurs around 40°N. In contrast, the difference between $\overline{MF_{max\_}B}$ and $\overline{MF_{HAWS}}$ is more pronounced. Across the latitudes of 40°S–35°N, $\overline{MF_{max\_}B}$ is generally smaller than both $\overline{MF_{max\_}A}$ and $\overline{MF_{HAWS}}$, only slightly exceeding the latter two in the 35°N–40°N region. The mean absolute difference between $\overline{MF_{max\_}B}$ and $\overline{MF_{HAWS}}$ across the latitudes of 40°S–40°N reaches 11.31×10^{-3}Pa. In the tropical region of 10°S–10°N , $\overline{MF_{max\_}B}$ is notably smaller than $\overline{MF_{HAWS}}$, with the maximum difference occurring near the equator, reaching 28.20×10^{-3}Pa , which is significantly larger than the maximum difference between $\overline{MF_{max\_}A}$ and $\overline{MF_{HAWS}}$. Figure 8 reveals that the difference between $\overline{MF_{max}}$ and $\overline{MF_{HAWS}}$ is primarily attributed to the pronounced discrepancy between $\overline{MF_{max\_}B}$ and $\overline{MF_{HAWS}}$, especially in the tropical region of 10°S–10°N.

https://doi.org/10.5194/egusphere-2026-2400
Preprint. Discussion started: 30 April 2026

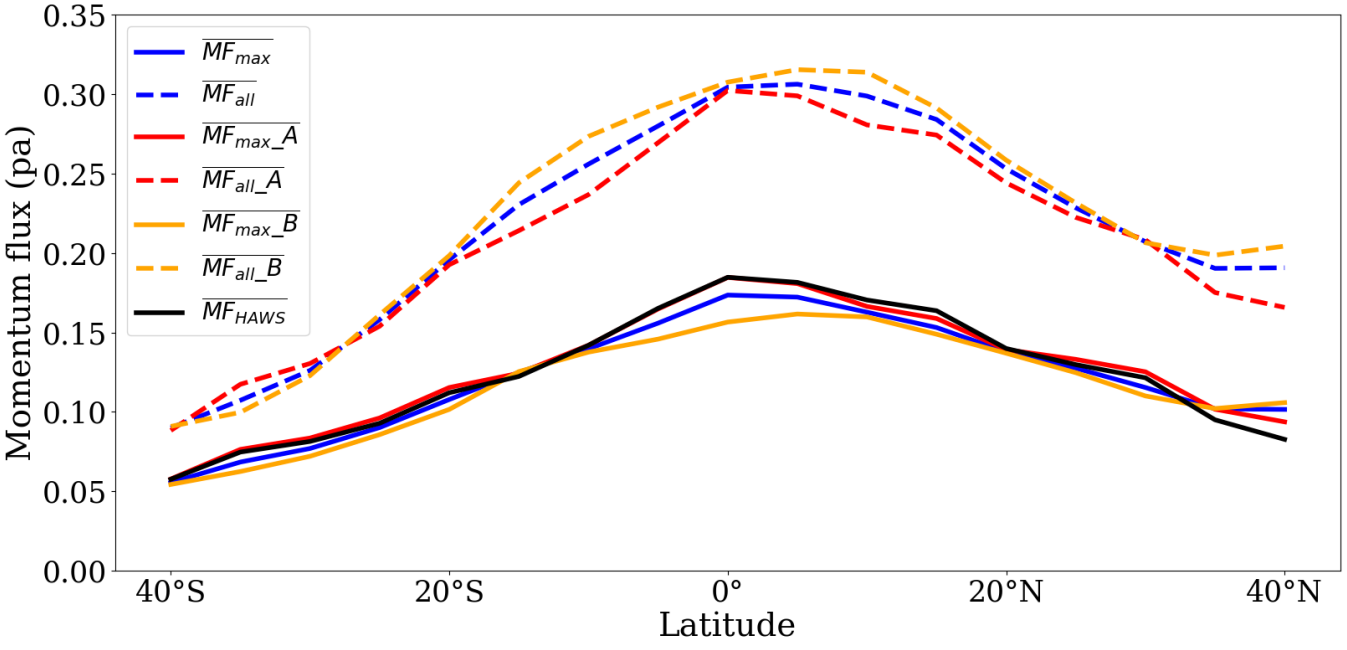

Figure 8: Latitudinal variations of zonal averaged momentum flux values retrieved from different types of triples and from all the triples.

Figure 8 also demonstrates that the peaks of both $\overline{MF_{all\_A}}$ and $\overline{MF_{max\_A}}$ occur near the equator, whereas the peaks of $\overline{MF_{all\_B}}$ and $\overline{MF_{max\_B}}$ are located near 10°N. As explained in Section 5.1.1, the low-latitude region of the NH hosts diverse and complex GW sources, which also leads to the existence of abundant Type B triples in this region. Although the amplitude profiles of these triples exhibit similar distributions of wave peaks, the vertical wavelengths corresponding to the maximum-amplitude wave signals may differ substantially (exceeding 2 km). These Type B triples, which are discarded by the traditional profile-triple-based method, are utilized by the proposed method and provide comprehensive GW MF information in this region. Furthermore, over most latitudes between 40°S–40°N, $\overline{MF_{all\_B}}$ exceeds $\overline{MF_{all\_A}}$, suggesting that the GW MF magnitude extracted from Type B triples surpasses that extracted from Type A triples in an overall sense.

6 Conclusions

This paper proposes a new method for retrieving multi-wave GW MF using GNSS RO dry temperature profile triples. The method begins by selecting dry temperature profile triples based on specified spatiotemporal constraints and extracting the temperature perturbation profiles. Subsequently, spectral analysis is performed on each triple of temperature perturbation profiles, and the high-amplitude vertical wavelength ranges of all the profiles in the triple are determined by setting an empirical threshold α, based on which an initial set of SVWs is obtained. For each SVW in the set, the horizontal wavelength of the corresponding wave signal is derived, and the MF of the signal is calculated if the horizontal wavelength

https://doi.org/10.5194/egusphere-2026-2400
Preprint. Discussion started: 30 April 2026

passes the quality check. The GW signal with the largest MF magnitude is defined as the primary GW signal, and the total MF magnitude is ultimately derived from the contributions of all GW signals associated with the final set of SVWs.

The value of the empirical threshold α directly influences the HAVWRs determined, which correspondingly affects the GW-related parameters retrieved subsequently. A strategy for selecting the optimal value of α is proposed. With this strategy, the mean differences in the zonal averaged total MF by applying adjacent α values with a fixed step size $\Delta\alpha$ were computed, and the optimal α value is selected as the one associated with the maximum variation in the differences. With the optimal setting of $\alpha = 0.6$, the new method is applied to all the COSMIC RO dry temperature profiles during June–August 2020, and GW MF magnitudes at different altitude levels over different latitudes between 40°S–40°N are retrieved and are compared with those obtained by the traditional profile-triple-based method.

By comparing the zonal averaged MF at different altitudes, it is found that the MF magnitude exhibits a decreasing trend with increasing altitude, a result consistent with existing studies. In the lower stratosphere of 20–25 km, the contribution of primary wave signals to the total MF magnitude is significantly lower than at altitudes above 25 km, and this is likely attributable to frequent wave-breaking processes and the generation of secondary GWs within 20–25 km, which relatively enhance the contribution of non-primary wave signals.

By classifying the qualified profile triples from which GW MF information is successfully extracted by the new method as two different types, the contributions of the two types of triples to the retrieval results are compared, and the differences in the MF retrieved by the proposed and the traditional methods are discussed. It is found that Type B triples, which are the qualified triples newly introduced by applying the new method, outnumber Type A triples, i.e., the triples satisfying the qualification criteria of the traditional method, and that the zonal averaged MF magnitudes of primary waves retrieved from Type A triples show good agreement with those obtained by the traditional method. Besides, in the tropical region of 10°S–10°N, the zonal averaged MF of primary waves from Type B triples is significantly smaller than that from Type A triples, and is also significantly smaller than that retrieved by the traditional method. Moreover, across most latitudes between 40°S–40°N, the zonal averaged total MF from Type B triples exceeds that from Type A triples, which is particularly pronounced around 20°N. This may be attributed to the complex GW sources around this latitude band, which leads to the existence of a substantial number of Type B triples.

In conclusion, the new method outperforms both the previous profile-pair-based retrieval method and the traditional profile-triple-based method. Compared with the profile-pair-based retrieval method of Wright and Gille (2013), the triple structure adopted in this study theoretically effectively avoids retrieval errors caused by inconsistencies between the profile-pair alignment direction and the actual propagation direction of GWs. Compared with the traditional profile-triple-based method, the advantage of the proposed method lies in two aspects, which are verified by the experiments carried out in the present work. First, by successfully extracting GW MF information from profile triples that would be discarded by the traditional method, the new method significantly improves data utilization of RO temperature profiles in GW MF retrieval. Second, by incorporating contributions from non-maximum-amplitude wave signals, the new method enhances the completeness and the reliability of the GW MF retrieval results. The total GW MF magnitude retrieved by the new method is

https://doi.org/10.5194/egusphere-2026-2400
Preprint. Discussion started: 30 April 2026

markedly higher than that obtained using the traditional profile-triple-based method, which is particularly pronounced in the low-latitude region of the NH, a phenomenon closely linked to the local impact factors of GW activities, such as monsoon activity, convective processes, and jet stream dynamics.

It should be noted that as pointed out in Section 5.1.3, the parameter selection approach for α proposed in the present study represents a preliminary scheme based on discrete sampling. Future work will focus on developing more advanced methods for the automatic determination of the threshold α to enhance the objectivity and applicability of the strategy.

Author contributions

JH: Methodology, Software, Data analysis, Writing – original draft, Visualization. JL: Conceptualization, Data curation, Software, Data analysis, Writing – review & editing, Supervision, Funding acquisition. XX: Conceptualization, Investigation, Writing – original draft, Writing – review & editing, Supervision, Funding acquisition.

Competing interests

The contact author has declared that none of the authors has any competing interests.

Code and data availability

The COSMIC-2 RO data can be accessed and downloaded at University Corporation for Atmospheric Research (UCAR) at https://data.cosmic.ucar.edu/gnss-ro/cosmic2/ (UCAR COSMIC Program, 2019). The code used to produce the results of this study is available from the corresponding authors upon qualified request.

Acknowledgements

We kindly acknowledge the COSMIC Data Analysis and Archive Center (CDAAC) at University Corporation for Atmospheric Research (UCAR) for providing the COSMIC-2 RO data.

Financial support

This study is supported by the National Natural Science Foundation of China under Grant Nos. 42174017, 41774033, 42074027, and 41774032.

https://doi.org/10.5194/egusphere-2026-2400
Preprint. Discussion started: 30 April 2026

References

Alexander, M. J., Gille, J., Cavanaugh, C., Coffey, M., Craig, C., Eden, T., Francis, G., Halvorson, C., Hannigan, J., Khosravi, R., Kinnison, D., Lee, H., Massie, S., Nardi, B., Barnett, J., Hepplewhite, C., Lambert, A., and Dean, V.: Global estimates of gravity wave momentum flux from High Resolution Dynamics Limb Sounder observations, J. Geophys. Res.-Atmos., 113, D15S18, https://doi.org/10.1029/2007JD008807, 2008.

Alexander, M. J., Geller, M., McLandress, C., Polavarapu, S., Preusse, P., Sassi, F., Sato, K., Eckermann, S., Ern, M., Hertzog, A., Kawatani, Y., Pulido, M., Shaw, T. A., Sigmond, M., Vincent, R., and Watanabe, S.: Recent developments in gravity wave effects in climate models and the global distribution of gravity wave momentum flux from observations and models, Q. J. Roy. Meteor. Soc., 136, 1103–1124, https://doi.org/10.1002/qj.637, 2010.

Alexander, M. J.: Global and seasonal variations in three dimensional gravity wave momentum flux from satellite limb-sounding temperatures, Geophys. Res. Lett., 42(16), 6860–6867, https://doi.org/10.1002/2015GL065234, 2015.

Alexander, M. J., Holton, J. R., and Durran, D. R.: The gravity wave response above deep convection in a squall line simulation, J. Atmos. Sci., 52, https://doi.org/10.1175/1520-0469(1995)052<2212:TGWRAD>2.0.CO;2, 1995.

Alexander, M. J. and Vincent, R. A.: Gravity waves in the tropical lower stratosphere: A model study of seasonal and interannual variability, J. Geophys. Res.-Atmos., 105(D14), 17983–17993, https://doi.org/10.1029/2000JD900197, 2000.

Alexander, P., de la Torre, A., Schmidt, T., Llamedo, P., and Hierro, R.: Limb sounders tracking topographic gravity wave activity from the stratosphere to the ionosphere around midlatitude Andes, J. Geophys. Res.-Space, 120, 9014–9022, https://doi.org/10.1002/2015JA021409, 2015.

Alexander, S. P. and Shepherd, M. G.: Planetary wave activity in the polar lower stratosphere, Atmos. Chem. Phys., 10(2), 707–718, https://doi.org/10.5194/acp-10-707-2010, 2010.

Andrews, D. G., Holton, J. R., and Leovy, C. B.: Middle atmosphere dynamics, Academic Press, 1987.

Anthes, R. A. and Schreiner, W. S.: Six new satellites watch the atmosphere over Earth's equator, Eos, 100, https://doi.org/10.1029/2019EO131779, 2019.

Ayorinde, T. T., Wrasse, C. M., Takahashi, H., Barros, D., Figueiredo, C. A. O. B., Lomotey, S. O., Essien, P., and Bilibio, A. V.: Stratospheric gravity wave potential energy and tropospheric parameters relationships over South America: a study using COSMIC-2 and METOP radio occultation measurements, Earth Planets Space, 75(1), 1–19, https://doi.org/10.1186/s40623-023-01891-8, 2023.

Babu, S. R. and Liou, Y. A.: Day-to-day variability of upper troposphere and lower stratosphere temperature in response to Taal volcanic eruption inferred from COSMIC-2 RO measurements, J. Volcanol. Geoth. Res., 421, 107445, https://doi.org/10.1016/j.jvolgeores.2021.107445, 2022.

Broutman, D. and Grimshaw, R.: The energetics of the interaction between short small-amplitude internal waves and inertial waves, J. Fluid Mech., 196, 93–106, https://doi.org/10.1017/S0022112088002629, 1988.

https://doi.org/10.5194/egusphere-2026-2400
Preprint. Discussion started: 30 April 2026

Ern, M., Preusse, P., Alexander, M. J., and Warner, C. D.: Absolute values of gravity wave momentum flux derived from satellite data, J. Geophys. Res., 109(20), D20103, https://doi.org/10.1029/2004JD004752, 2004.

Ern, M., Preusse, P., Gille, J. C., Hepplewhite, C. L., Mlynczak, M. G., Russell III, J. M., and Riese, M.: Implications for atmospheric dynamics derived from global observations of gravity wave momentum flux in stratosphere and mesosphere, J. Geophys. Res., 116(D19), D19107, https://doi.org/10.1029/2011JD015821, 2011.

Faber, A., Llamedo, P., Schmidt, T., de la Torre, A., and Wickert, J.: On the determination of gravity wave momentum flux from GPS radio occultation data, Atmos. Meas. Tech., 6(11), 3169–3180, https://doi.org/10.5194/amt-6-3169-2013, 2013.

Fels, S. B.: The radiative damping of short vertical scale waves in the mesosphere, J. Atmos. Sci., 41, 1755–1764, https://doi.org/10.1175/1520-0469(1984)041<1755:TRDOSV>2.0.CO;2, 1984.

Fritts, D. C. and Alexander, M. J.: Gravity wave dynamics and effects in the middle atmosphere, Rev. Geophys., 41, 1003, https://doi.org/10.1029/2001RG000106, 2003.

Geller, M. A., Alexander, M. J., Love, P. T., Bacmeister, J., Ern, M., Hertzog, A., Manzini, E., Preusse, P., Sato, K., Scaife, A. A., and Zhou, T.: A comparison between gravity wave momentum fluxes in observations and climate models, J. Climate, 26, 6383–6405, https://doi.org/10.1175/JCLI-D-12-00545.1, 2013.

Hei, H., Tsuda, T., and Hirooka, T.: Characteristics of atmospheric gravity wave activity in the polar regions revealed by GPS radio occultation data with CHAMP, J. Geophys. Res., 113(D4), D04107, https://doi.org/10.1029/2007JD008938, 2008.

Hindley, N. P., Wright, C. J., Smith, N. D., and Mitchell, N. J.: The southern stratospheric gravity wave hot spot: individual waves and their momentum fluxes measured by COSMIC GPS-RO, Atmos. Chem. Phys., 15(3), 7797–7818, https://doi.org/10.5194/acp-15-7797-2015, 2015.

Hocke, K. and Tsuda, T.: Gravity waves and ionospheric irregularities over tropical convection zones observed by GPS/MET radio occultation, Geophys. Res. Lett., 28(14), 2815–2818, https://doi.org/10.1029/2001GL013076, 2001.

Holton, J. R.: The role of gravity wave induced drag and diffusion in the momentum budget of the mesosphere, J. Atmos. Sci., 39(4), 791–799, https://doi.org/10.1175/1520-0469(1982)039<0791:TROGWI>2.0.CO;2, 1982.

Holton, J. R.: The influence of gravity wave breaking on the general circulation of the middle atmosphere, J. Atmos. Sci., 40(10), 2497–2507, https://doi.org/10.1175/1520-0469(1983)040<2497:TIOGWB>2.0.CO;2, 1983.

Horinouchi, T. and Tsuda, T.: Spatial structures and statistics of atmospheric gravity waves derived using a heuristic vertical cross-section extraction from COSMIC GPS radio occultation data, J. Geophys. Res.-Atmos., 114, D16110, https://doi.org/10.1029/2008JD011068, 2009.

Jana, S., Rakshit, G., and Maitra, A.: Gravity wave activities associated with convective phenomena at a tropical location near land-sea boundary, Radio Sci., 55, e2019RS006952, https://doi.org/10.1029/2019RS006952, 2020.

John, S. R. and Kumar, K. K.: TIMED/SABER observations of global gravity wave climatology and their interannual variability from stratosphere to mesosphere lower thermosphere, Clim. Dynam., 39(6), 1489–1505, https://doi.org/10.1007/s00382-012-1329-9, 2012.

https://doi.org/10.5194/egusphere-2026-2400
Preprint. Discussion started: 30 April 2026

Kim, Y. J., Eckermann, S. D., and Chun, H. Y.: An overview of the past, present and future of gravity-wave drag parametrization for numerical climate and weather prediction models, Atmos.-Ocean, 41(1), 65–98, https://doi.org/10.3137/ao.410105, 2003.

Kursinski, E. R., Hajj, G. A., Schofield, J. T., Linfield, R. P., and Hardy, K. R.: Observing Earth's atmosphere with radio occultation measurements using the Global Positioning System, J. Geophys. Res.-Atmos., 102(D19), 23429–23465, https://doi.org/10.1029/97JD01569, 1997.

Lindzen, R. S.: Turbulence and stress owing to gravity wave and tidal breakdown, J. Geophys. Res.-Oceans, 86(C10), 9707–9714, https://doi.org/10.1029/JC086iC10p09707, 1981.

Liu, X., Yue, J., Xu, J., Garcia, R. R., Russell III, J. M., Mlynczak, M., Wu, D. L., and Nakamura, T.: Variations of global gravity waves derived from 14 years of SABER temperature observations, J. Geophys. Res.-Atmos., 122, 6231–6249, https://doi.org/10.1002/2017JD026604, 2017.

Meriwether, J. W. and Gerrard, A. J.: Mesosphere inversion layers and stratosphere temperature enhancements, Rev. Geophys., 42(3), https://doi.org/10.1029/2003RG000133, 2004.

Pedatella, N. M., Zakharenkova, I., Braun, J. J., Cherniak, I., Hunt, D., Schreiner, W. S., Straus, P. R., Valant-Weiss, B. L., Vanhove, T., Weiss, J., and Wu, Q.: Processing and validation of FORMOSAT-7/COSMIC-2 GPS total electron content observations, Radio Sci., 56, e2021RS007267, https://doi.org/10.1029/2021RS007267, 2021.

Preusse, P., Ern, M., Eckermann, S. D., Warner, C. D., Picard, R. H., Knieling, P., Krebsbach, M., Russell III, J. M., Mlynczak, M. G., Mertens, C. J., and Riese, M.: Tropopause to mesopause gravity waves in August: Measurement and modelling, J. Atmos. Sol.-Terr. Phy., 68(15), 1730–1751, https://doi.org/10.1016/j.jastp.2005.10.019, 2006.

Rakshit, G., Jana, S., and Maitra, A.: Gravity wave behavior in lower stratosphere during tropical cyclones over the Bay of Bengal, Radio Sci., 53, 1356–1367, https://doi.org/10.1029/2018RS006614, 2018.

Randel, W. J., Wu, F., and Podglajen, A.: Equatorial waves, diurnal tides and small-scale thermal variability in the tropical lower stratosphere from COSMIC-2 radio occultation, J. Geophys. Res.-Atmos., 126(7), e2020JD033969, https://doi.org/10.1029/2020JD033969, 2021.

Ratnam, M. V., Tetzlaff, G., and Jacobi, C.: Global and seasonal variations of stratospheric gravity wave activity deduced from the CHAMP/GPS satellite, J. Atmos. Sci., 61, 1610–1620, https://doi.org/10.1175/1520-0469(2004)061<1610:GASVOS>2.0.CO;2, 2004.

Ratnam, M. V., Babu, A. N., Rao, V. V. M. J., Rao, S. V. B., and Rao, D. N.: MST radar and radiosonde observations of inertia gravity wave climatology over tropical stations: Source mechanisms, J. Geophys. Res.-Atmos., 113, D07109, https://doi.org/10.1029/2007JD008986, 2008.

Savitzky, A. and Golay, M.: Smoothing and differentiation of data by simplified least squares procedures, Anal. Chem., 36(8), 1627–1639, https://doi.org/10.1021/ac60214a047, 1964.

Schmidt, T., Alexander, P., and de la Torre, A.: Stratospheric gravity wave momentum flux from radio occultations, J. Geophys. Res.-Atmos., 121(9), 4443–4467, https://doi.org/10.1002/2015JD024135, 2016.

https://doi.org/10.5194/egusphere-2026-2400
Preprint. Discussion started: 30 April 2026

Schreiner, W. S., Weiss, J. P., Anthes, R. A., Braun, J., Chu, V., Fong, J., Hunt, D., Kuo, Y.-H., Meehan, T., Serafino, W., Sjoberg, J., Sokolovskiy, S., Talaat, E., Wee, T. K., and Zeng, Z.: COSMIC-2 radio occultation constellation: First results, Geophys. Res. Lett., 47, e2019GL086841, https://doi.org/10.1029/2019GL086841, 2020.

Steiner, A. K. and Kirchengast, G.: Error analysis for GNSS radio occultation data based on ensembles of profiles from end-to-end simulations, J. Geophys. Res., 110(D15), D15307, https://doi.org/10.1029/2004JD005251, 2005.

Sutherland, B. R.: Internal wave reflection in uniform shear, Q. J. Roy. Meteor. Soc., 126, 3255–3287, https://doi.org/10.1002/qj.49712657013, 2000.

Sutherland, B. R.: Finite-amplitude internal wavepacket dispersion and breaking, J. Fluid Mech., 429, 343–380, https://doi.org/10.1017/S0022112000002846, 2001.

Torrence, C. and Compo, G. P.: A practical guide to wavelet analysis, B. Am. Meteorol. Soc., 79(1), 61–78, https://doi.org/10.1175/1520-0477(1998)079<0061:APGTWA>2.0.CO;2, 1998.

Tsuda, T., Nishida, M., Rocken, C., and Ware, R. H.: A global morphology of gravity wave activity in the stratosphere revealed by the GPS occultation data (GPS/MET), J. Geophys. Res., 105(D6), 7257–7273, https://doi.org/10.1029/1999JD901005, 2000.

UCAR COSMIC Program: COSMIC-2 Data Products [Data set]. UCAR/NCAR - COSMIC, https://doi.org/10.5065/T353-C093, 2019

Vincent, R. A. and Alexander, M. J.: Gravity waves in the tropical lower stratosphere: An observational study of seasonal and interannual variability, J. Geophys. Res.-Atmos., 105, 17983–17993, https://doi.org/10.1029/2000JD900197, 2000.

Wang, L. and Alexander, M. J.: Global estimates of gravity wave parameters from GPS radio occultation temperature data, J. Geophys. Res.-Atmos., 115, D21122, https://doi.org/10.1029/2010JD013860, 2010.

Wright, C. J. and Gille, J. C.: HIRDLS observations of gravity wave momentum fluxes over the monsoon regions, J. Geophys. Res., 116, D12103, https://doi.org/10.1029/2011JD015725, 2011.

Wright, C. J. and Gille, J. C.: Detecting overlapping gravity waves using the S-Transform, Geophys. Res. Lett., 40, 1850–1855, https://doi.org/10.1002/grl.50378, 2013.

Zeng, X., Peng, Y., and Liu, S.: Three-dimensional analysis of global gravity waves based on COSMIC multi-satellite observations, Geophys. Res. Lett., 48, e2021GL094809, https://doi.org/10.1029/2021GL094809, 2021.

Zhang, Y., Zhang, S., Huang, C., Huang, K., Gong, Y., and Gan, Q.: The interaction between the tropopause inversion layer and the inertial gravity wave activities revealed by radiosonde observations at a midlatitude station, J. Geophys. Res.-Atmos., 120, 8099–8111, https://doi.org/10.1002/2015JD023115, 2015.

Zhu, X.: A new theory of the saturated gravity wave spectrum for the middle atmosphere, J. Atmos. Sci., 51, 3615–3626, https://doi.org/10.1175/1520-0469(1994)051<3615:ANTOTS>2.0.CO;2, 1994.